Check for updates

Received: 11 November 2022 | Revised: 19 May 2023 | Accepted: 5 July 2023

DOI: 10.1002/joc.8188

RESEARCH ARTICLE

International Journal of Climatology RMetS

Diurnal to interannual variability of low-level cloud cover over western equatorial Africa in May–October

Vincent Moron[1,2] | **P. Camberlin**[3] | **R. Aellig**[4] | **O. Champagne**[5] | **A. H. Fink**[4] | **P. Knippertz**[4] | **N. Philippon**[5]

[1]Aix-Marseille University, CNRS, IRD, INRAE, Collège de France CEREGE, Aix-en-Provence, France

[2]International Research Institute for Climate and Society, Lamont-Doherty Earth Observatory, Columbia University, Palisades, New York, USA

[3]Biogéosciences/CRC, Université Bourgogne Franche-Comté/CNRS, Dijon, France

[4]Institute of Meteorology and Climate Research, Karlsruhe Institute of Technology, Karlsruhe, Germany

[5]Institut des Géosciences de l'Environnement, UGA, CNRS, IRD, Grenoble INP, Grenoble, France

Correspondence

Vincent Moron, Aix-Marseille University, CNRS, IRD, INRAE, Collège de France CEREGE, Aix-en-7 Provence, France.
Email: moron@cerege.fr

Funding information

Agence Nationale de la Recherche, Grant/Award Number: ANR-19-CE01-0021; Deutsche Forschungsgemeinschaft, Grant/Award Number: DFG FI 786/5-1

Abstract

This study examines the diurnal to interannual variations of the stratiform cloud cover in May–October (1971–2019) from a 3-hourly station database and from ERA5 reanalyses over western equatorial Africa (WEA). The main diurnal variations of the local-scale fraction and genus of stratiform clouds are synthesized into three canonical diurnal types (i.e., "clear," "clear afternoon," "cloudy" days). The interannual variations of frequencies of the three diurnal types during the cloudiest months (JJAS) are mostly associated with two main mechanisms: a meridional shallow overturning cell associating more "cloudy" and less "clear" and "clear afternoon" days to anomalous southerlies below 900 hPa over and around WEA, anomalous ascent around 5°–7°N, anomalous northerlies between 875 and 700 hPa, and anomalous subsidence over the equatorial Atlantic. This circulation is strongly related to interannual variations of the equatorial Atlantic upwelling (i.e., more clouds when the upwelling is strong) associated with a meridional shift of the Intertropical Convergence Zone over the Tropical Atlantic and adjacent continents. The second mechanism operates mostly in the zonal direction and involves again the coupled ocean–atmosphere system over the equatorial Atlantic, but also the remote El Niño–Southern Oscillation (ENSO). An anomalously cold equatorial Atlantic drives increased low-level westerlies toward the Congo Basin. Warm ENSO events promote broad warm and easterly anomalies in the middle and upper troposphere, which increase the local static stability, and thus the local stratiform cloud cover over WEA. The present study suggests new mechanisms responsible for interannual variations of stratiform clouds in WEA, thus providing avenues of future research regarding the stability of the stratiform cloud deck under the ongoing differential warming of tropical ocean and land masses.

KEYWORDS

atmosphere, cold tongue, ERA5, stratiform cloud, surface observation

---

1 | INTRODUCTION

Western equatorial Africa (WEA), comprising the countries of Equatorial Guinea, Gabon, the southwestern part of the Republic of Congo (RC) and southern Cameroon (∼5°S–5°N, west of 15°E), exhibits an almost absolute dry season centred on June–September combined with a persistent low-level cloud cover. The low-level cloud cover fractions (LCF) usually exceed 70%–80% over the coastal area and first hills and plateaus (Champagne et al., 2023; Dommo et al., 2018), strongly limiting the incoming solar radiation at the surface (Philippon et al., 2019, 2022), the maximum diurnal temperature range and the evapotranspiration rate (Philippon et al., 2019) with major impacts on forest functioning and composition (Réjou-Méchain et al., 2021).

A compact, stratiform cloud deck, with light precipitation or drizzle at best, is relatively rare over the continents, but rather common over the oceans below the eastern edges of the subtropical and tropical oceanic anticyclones, where the subsiding branches of the Hadley and Walker cells are co-located with cold currents flowing over the eastern sides of ocean basins (Eastman et al., 2011; Eastman & Warren, 2014; Weare, 2000; Wood, 2012). Continental stratiform cloud decks are sometimes found close to the Equator as in northern Peru and Ecuador (Bendix et al., 2006), or along the Guinea Coast in western Africa during the "little" dry season in boreal summer (Knippertz et al., 2011; van der Linden et al., 2015). None of these, however, can rival the peak in mean annual stratiform cloudiness over WEA with its very strong annual cycle (Wood, 2012). In the subequatorial regions of stratiform clouds, the cold sea surface temperatures (SSTs) promote a strong low-level thermal inversion and increase the dry static stability (usually referred to as lower tropospheric stability [LTS]) over the seas and downstream (Eastman & Warren, 2013, 2014; Klein & Hartmann, 1993; Klein et al., 1995; Koshiro & Shiotani, 2014; Norris, 1998a, 1998b; Norris & Leovy, 1994; Oreopoulos & Davies, 1993; Park & Leovy, 2004; Wood, 2012; Wood & Bretherton, 2006; Zhang et al., 2009), while the stratiform deck may also feedback on SSTs through suppressed surface radiation (Solmon et al., 2021). At the seasonal and interannual time scales, the variations of marine stratus clouds are expected to closely follow those of the LTS strength (Eastman & Warren, 2013; Klein & Hartmann, 1993; Wood, 2012) and, consequently, being out-of-phase with local SSTs.

In WEA, the amount of stratiform clouds is likely dependent on the strength of the seasonal coastal and equatorial upwelling in the eastern tropical Atlantic Ocean (between roughly 4°S and 1°N) where the amplitude of the annual cycle is especially large (Merle et al., 1979). The seasonal upwelling is concomitant with the intensification, mostly from May, of the trade winds originating from the southern hemisphere in relation to the developing boreal summer monsoon over West Africa (Caniaux et al., 2011; Li & Philander, 1997; Wang et al., 2017) and the synchronous intensification and northward migration of the St. Helena anticyclone (Caniaux et al., 2011; de Coëtlogon et al., 2010; Meynadier et al., 2016). The Atlantic equatorial and coastal upwelling is also known to be related to the excitation of equatorial Kelvin waves further west, through the above-mentioned seasonal enhancement of the trades (Berrit, 1976; Merle et al., 1979; Moore et al., 1978; Picaut, 1983; Wang et al., 2017).

In austral winter, a vertical wind shear is observed over WEA between an oceanic cool low-level flow, diverging between south-southeasterly winds over the Atlantic Ocean and west-southwesterly winds over WEA, and weak to moderate easterly winds above ∼850 hPa (i.e., Nicholson & Grist, 2003). These easterlies provide relatively warm, but also moist, air above WEA. The southerly meridional component of the low-level winds over equatorial Atlantic and coastal WEA could be interpreted as the lower branch of the regional-scale southern hemisphere Hadley cell. A relationship has already been established between the development of the equatorial cold tongue and the first wet season across the Guinean coast of West Africa during the boreal spring, through the shallow low-level atmospheric circulation (LLAC) described by Leduc-Leballeur et al. (2013) and Meynadier et al. (2016). LLAC links the start of the first rainy season over the Guinean Africa (Sultan & Janicot, 2003) with an increased meridional gradient in mean sea level pressure induced by the strengthened meridional SST gradient along the northern front of the intensifying equatorial cold tongue (de Coëtlogon et al., 2010; Leduc-Leballeur et al., 2013) contrasting with warm SST trapped in the Bight of Bonny. The westerly zonal component of the low-level winds over WEA is usually interpreted as the lower branch of a seasonal (roughly from June to October) zonal overturning cell established between the equatorial cold tongue and the warmer Congo Basin. Over the latter, at around 20°–30°E, the near-equatorial convection and rainfall is substantial, even during the austral winter dry season (Cook & Vizy, 2016; Neupane, 2016; Pokam et al., 2014). According to Neupane (2016) and Longandjo and Rouault (2020), an easterly return flow occurs at and above 800 hPa, thus defining a shallow zonal cell with low-level westerlies, and may add to the meridional Hadley cell-related subsidence above the cold equatorial Atlantic SSTs. Cook and Vizy (2016) refer to a deep Walker cell-type circulation, which intensifies when the eastern Atlantic SSTs is anomalously warm, enhancing moisture transport toward the Congo Basin, in contrast with the shallow zonal Congo overturning cell which is intensified through an enhanced zonal thermal gradient, for example when equatorial Atlantic SSTs is anomalously cold.

The main goals of this study are to depict the diurnal to interannual and longer space–time variations of the stratiform cloud cover over WEA and their relationships to SST and atmospheric conditions. We used a multidecadal database of station-based LCF and low-level cloud genus (LCG) used in the recent study of Champagne et al. (2023) to document first the diurnal and seasonal variations during the extended cloudy dry season from May to October 1971–2019 (Dommo et al., 2018). The main mode of local-scale diurnal variations will be synthesized using three canonical diurnal types and then their seasonal frequency during the cloudiest months (June–September) will be analysed at interannual time scale. In particular, we will establish if the relationships between low-level cloud cover and SST found in previous studies mentioned above for the tropical oceanic regions are transferable to continental WEA. Section 2 presents the data in more detail. Section 3 contains the space–time analysis of stratiform cloud cover over WEA at diurnal and seasonal time scales starting from the definition of the three diurnal types. Section 4 analyses the interannual variability through the relationships between the leading empirical orthogonal function of the cloudiest season (i.e., JJAS) frequencies of the three diurnal types and potential tropical and regional oceanic–atmospheric drivers. Section 5 discusses the main mechanisms operating at interannual time scales and section 6 concludes the paper.

2 | DATA

2.1 | Observed low-level cloud cover

The primary dataset is the Extended Edited Cloud Report Archive (EECRA; Eastman et al., 2011; Eastman & Warren, 2013; Hahn & Warren, 2009). It provides verified 3-hourly (0000, 0300 UTC, etc.) LCF (in oktas) and LCG (the nine low cloud genera defined by the WMO standards plus two extra categories [#10: "sky obscured by fog" and #11: "cumulonimbus with thunderstorm"]) as well as many meteorological characteristics over 85 synoptic stations in the 1971–2009 period. This primary EECRA dataset has been completed by various sources, detailed in Champagne et al. (2023), leading to a consistent quality-controlled database of 3-hourly LCF and LCG observed at 88 stations (Figure 1) in the May to October 1971–2019 period (Aellig et al., 2022). Three stations unavailable in EECRA have also been added. Note that these three stations are used in the climatological maps (Figure 3a–f), but not in the subsample of 26 homogenized stations used to define the diurnal types (see section 3.2) and to analyse the interannual variability of LCF. As the two extra EECRA categories of LCF are very rare in our database (<0.1% of the available entries) and not available in the other sources, we restricted our analysis to LCG 1–9. LCG#10 and #11 from EECRA have been set to missing entries. Moreover, we restricted our analysis to stratiform clouds (mostly stratocumulus on WEA; Champagne et al., 2023) by resetting LCF to zero for LCG 1–3 and 9 (i.e., cumulus and cumulo-nimbus with or without anvils), such that the low bases of cumuliform clouds are not mixed with stratiform clouds. So in the following, LCF should be interpreted as stratiform only LCF, while LCG documents all genus of low clouds including bases of cumuliform clouds.

Possible heterogeneities in the stratiform LCF timeseries at the the most complete 26 stations (Figure 2) have been assessed using the Standard Normal Homogeneity Test (SNHT; Alexandersson & Moberg, 1997). In the case of clouds and cloudiness, the main source of heterogeneity is the change of observer or observing practices, since in WEA cloudiness data at all the stations is derived from visual observations only. SNHT involves computing the difference between standardized LCF timeseries from each candidate station (Y in Figure 2) and a reference LCF timeseries (S in Figure 2). Here, the reference timeseries is a weighted average of five major synoptic stations with relatively uninterrupted LCF timeseries, namely Libreville, Port-Gentil, Brazzaville, Pointe-Noire and Ouesso (Figure 1), and representative of different climate regions. Note that ERA5 LCF data (see section 2.2) were also tested as a reference, but the correlations with the reference timeseries were much lower, causing more uncertainty in the results. The SNHT statistic is compared against critical values (Alexandersson & Moberg, 1997; Khaliq & Ouarda, 2007), which enables detecting artificial breakpoints in the candidate timeseries. The tests were carried out on the May–October seasonal mean and on each individual month in order to retain only the most consistent breakpoints. With an additional visual inspection of the timeseries, spurious breakpoints were found at Mouila (2010) (Figure 2), Lambaréné (2015), Bitam (1978 and 2013), Tchibanga (1985), Mitzic (1998) and Moanda (1996). The LCF timeseries for each 3-h time-slot at these stations were thereafter homogenized. This was done by subtracting from the shorter subperiod (before or after the breakpoint) the difference between the mean LCF of the two subperiods in the candidate timeseries, with respect to each breakpoint

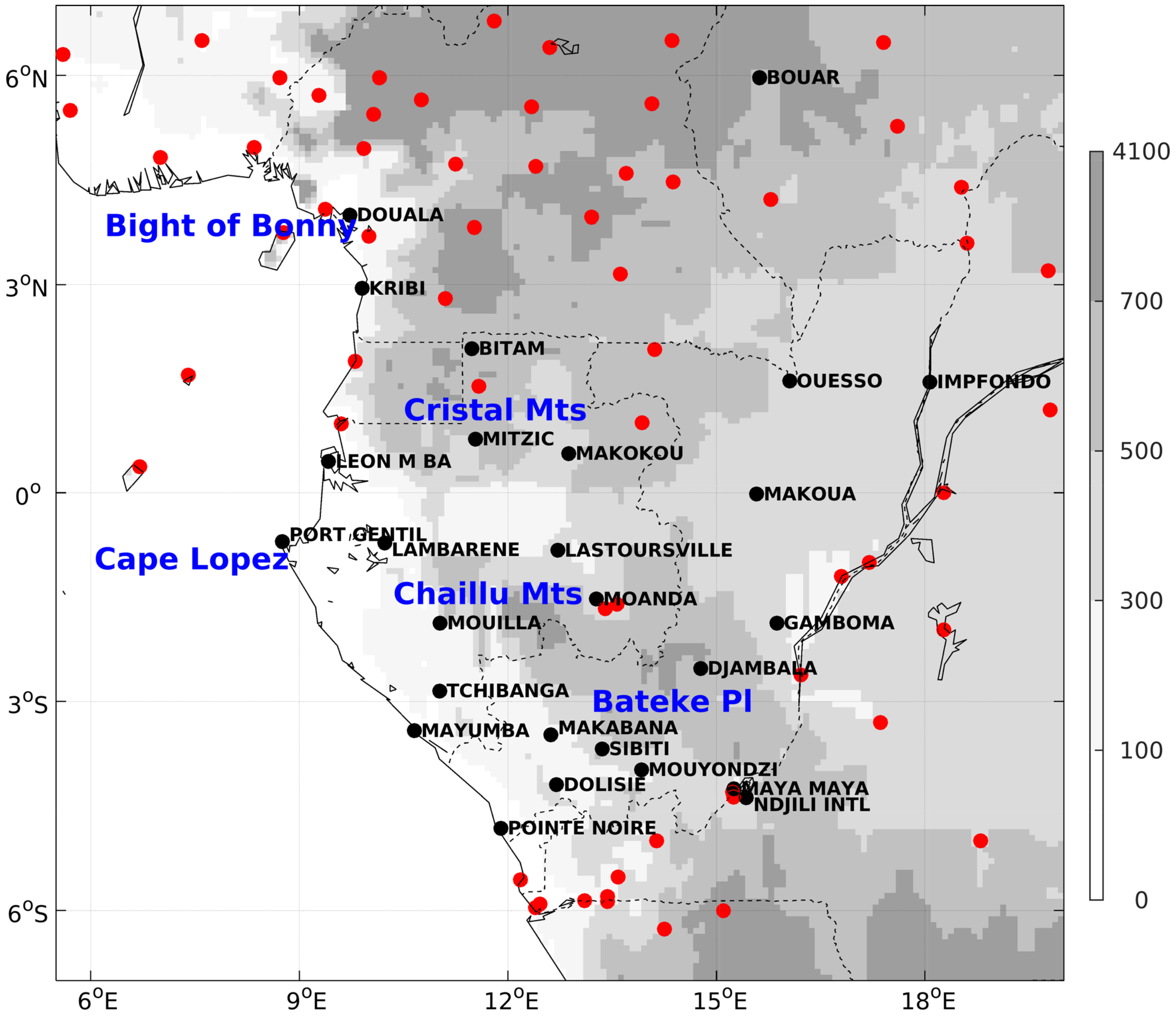

FIGURE 1 Topography (grey shadings in meter asl) and location of the 26 stations (named black dots) used in most of the analyses. The stations of the original data set (Aellig et al., 2022; Champagne et al., 2023) used for climatology only (Figure 3) are plotted as unnamed red dots [Colour figure can be viewed at wileyonlinelibrary.com]

year, minus the difference between the same two subperiods in the reference timeseries.

2.2 | ERA5 low-level cloud cover

Clouds in ERA5 are taken from short-term model forecasts and thus are not directly affected by assimilated observations. Our first goal is to check the accuracy of ERA5 to reproduce realistic space–time low cloud cover variations from diurnal to interannual time scales. If successful, this is also an indirect way to check if any hidden heterogeneities in the observations have a discernible impact on our analyses. Three-hourly ERA5 LCF (varying between 0 and 1) is defined for clouds below ~800 hPa (exactly 0.8 * surface pressure), thus potentially mixing stratiform clouds with convective clouds with a low cloud base, such as cumulo-nimbus. We tested two different preprocessings in section 3.1 to correct this potential bias.

2.3 | Additional data

All monthly atmospheric data and sea or land surface temperature were extracted from ERA5 (Hersbach et al., 2020) for the full period 1971–2019 at a horizontal resolution of 0.25°. Note that monthly mean values of

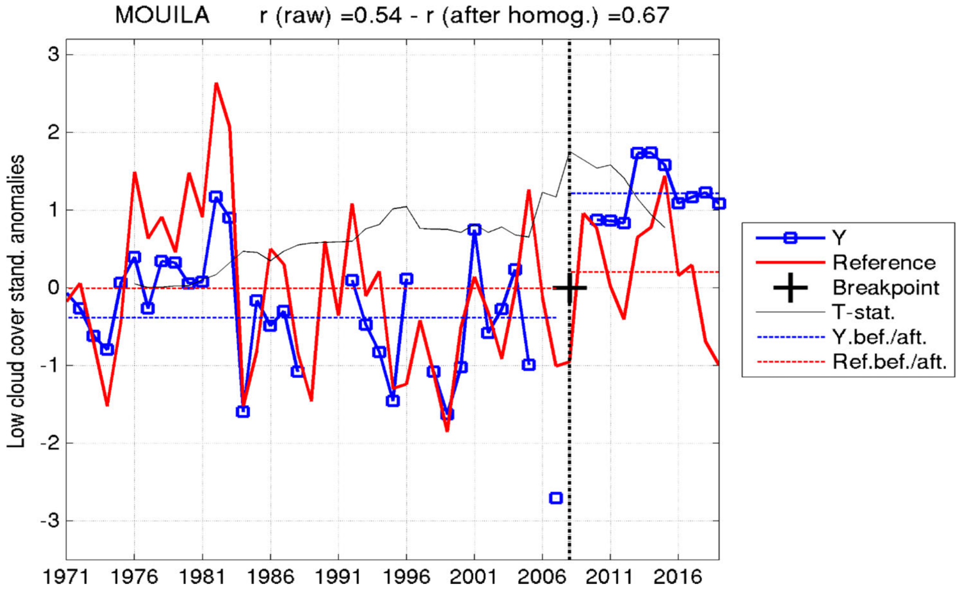

FIGURE 2 An example of homogeneity testing of the Mouila (Gabon) LCF timeseries (JJAS mean), showing raw timeseries (blue line and squares), reference timeseries (red line), identified breakpoint (cross) and values of the *t* statistic (thin black line). Dashed lines show the average for the subperiods before and after the breakpoints (blue: raw timeseries, red: reference timeseries) [Colour figure can be viewed at wileyonlinelibrary.com]

ERA5 are computed from 0000 UTC only. Lastly, monthly rainfall is extracted from GPCP v2.3 (available from 1979 only) at a horizontal resolution of 1° (Adler et al., 2018) to look at the relationships between the interannual variations of LCF and the large-scale rainfall patterns over the global Tropics, including the location and intensity of the InterTropical Convergence Zone (ITCZ) and the associated rainbelt around and over the Atlantic Ocean and African continent.

3 | SPACE–TIME VARIATIONS OF THE STRATIFORM CLOUD DECK

3.1 | Monthly mean climatology and reliability of low-level cloud cover from ERA5

Figure 3a–f shows the monthly mean climatologies for the observed (dots) and ERA5 (shadings) LCF. LCF peaks from southwestern Cameroon to the coasts of the Democratic Republic of Congo in July–August as already demonstrated by Dommo et al. (2018). The prefiltering of ERA5 data using the convective rainfall minimizes the spatially averaged bias and maximizes ERA5 pattern correlations with observations (Table 1). The improvement versus raw ERA5 LCF is especially clear from southeastern Nigeria and the Bight of Bonny to the southwestern Central African Republic (CAR) and northern RC across southern Cameroon, where deep convection is still occurring in boreal summer (not shown).

Figure 3g–l shows the station-scale correlations of observed and ERA5 interannual variations of monthly mean LCF anomalies. ERA5 and observations are closer for stations recording the largest LCF, while correlations decrease over the northern RC (Figure 3g–l). Correlations tend also to decrease from July to October. There are no large differences among the different versions of ERA5 LCF tested meaning that the interannual LCF variations are robust (Table 1).

Regional-scale interannual variations of monthly LCF are explored through a standardized anomaly index (SAI; Katz & Glantz, 1986), defined as the weighted average of local LCF standardized anomalies (zero mean and unit variance) across the 16 stations belonging to the cloudiest area (2°N–6°S, W of 14°E) outlined in Figure 3g. SAI weights (Osborn et al., 1997) consider both the varying number of available stations in each year so as not to bias the interannual variations, which are noisier when less stations are available, and the mean cross-correlations among available stations, so that the spatially consistent variations are emphasized in the SAI. The 1971–2019 linear trend for observed LCF and ERA5 LCF is also shown. The temporal behaviour of ERA5 monthly LCF is largely consistent with that of observations (Figure 4). Despite some intraseasonal differences, the correlations are far larger than at the local scale (Table 1), as expected from the cancellation of near-independent variations between neighbouring stations due to the spatial averaging. The correction using the convective rainfall ≥0.1 mm provides the best fit to observations for all months considered (Table 1) and is thus retained for the next analyses.

3.2 | Definition of low-level cloud cover diurnal types

The analysis of interannual variations is not as trivial as the one of diurnal and seasonal cycles, which are very strong in amplitude and well sampled. There are three

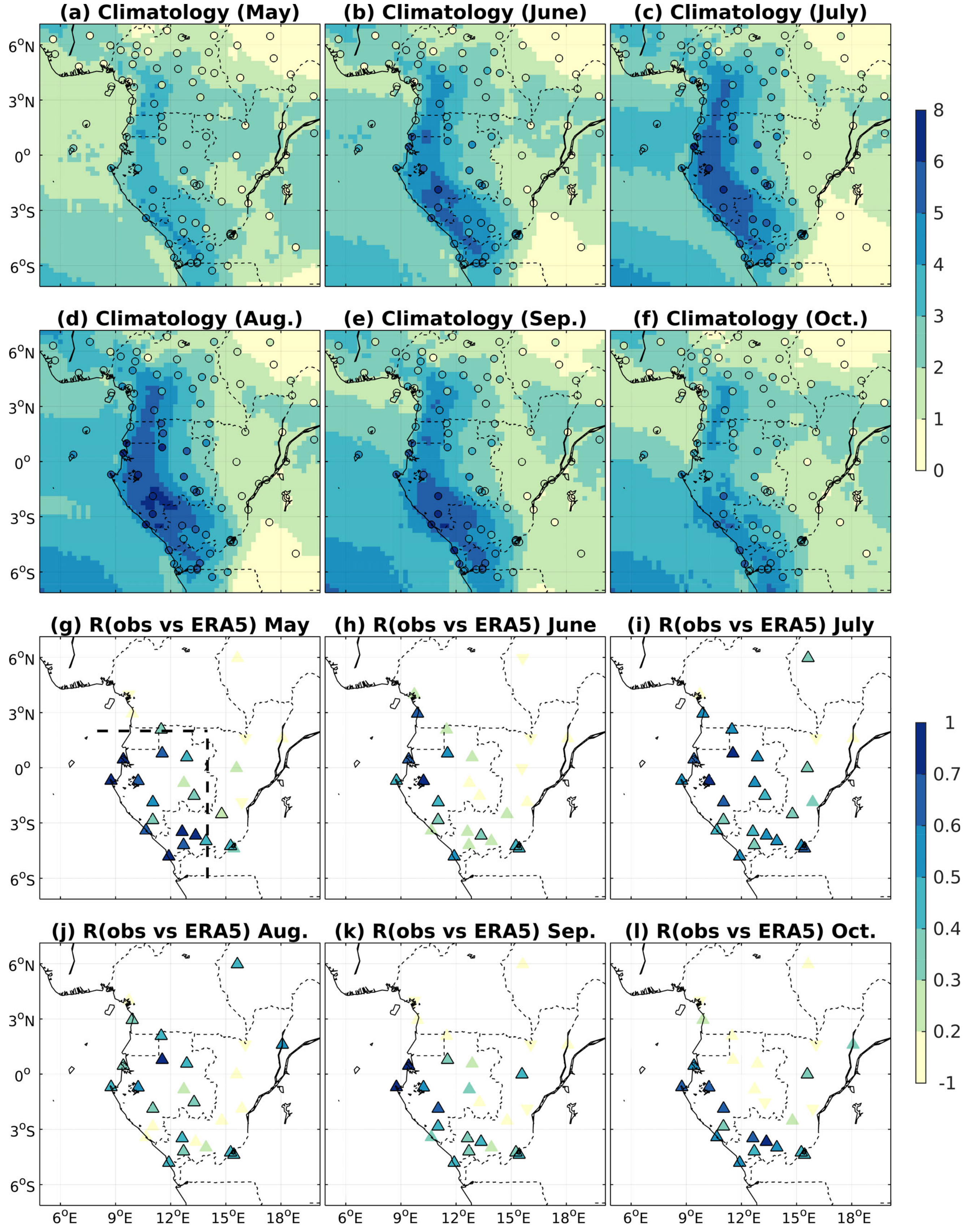

FIGURE 3 Legend on next page.

TABLE 1 Accuracy of monthly mean ERA5 LCF space–time variations with respect to observed one

	May	June	July	August	September	October
p.c. raw	0.62	0.66	0.67	0.73	0.76	0.78
p.c. CR	**0.72**	**0.83**	**0.85**	**0.84**	**0.82**	**0.80**
p.c. MCF	0.63	0.71	0.77	0.80	0.80	0.79
bias raw	1.4	1	0.6	0.7	1.2	1.4
bias CR	**0.4**	**0.2**	−0.3	−0.2	**0**	**0.1**
bias MCF	1.1	0.6	**0**	**0.1**	0.6	0.9
corr. raw	0.29	**0.34**	**0.45**	0.30	0.28	**0.30**
corr. CR	**0.33**	0.32	0.43	**0.32**	**0.29**	0.29
corr. MCF	0.26	0.32	0.41	0.25	0.25	0.26
corr. SAI raw	0.79	**0.66**	0.75	0.55	0.79	0.72
corr. SAI CR	**0.83**	**0.66**	**0.76**	**0.58**	**0.80**	**0.81**
corr. SAI MCF	0.75	0.63	0.73	0.50	0.73	0.72

Note: "p.c." is pattern correlation between mean climatologies at the 88 observed stations and their corresponding nearest ERA5 grid-point. "bias" is the spatially averaged bias (in oktas) of ERA5 versus observations. "corr" is the correlation between observed and ERA5 LCF spatially averaged over the 26 stations shown in Figure 3g–l. "corr SAI" is the correlation between observed and ERA5 LCF standardized anomaly index computed from the 16 stations over Gabon and SW of the Republic of Congo (dashed box in Figure 3g). "raw" means unfiltered ERA5 LCF while "CR" and "MCF" means filtered ERA5 LCF using, respectively, the convective rainfall (3-hourly LCF is set to zero when 3-hourly convective rainfall $\geq$0.1 mm·h^{-1}) and the middle level cloud fraction (3-hourly LCF is set to zero if 3-hourly middle level cloud fraction >LCF). In each block of three rows, the bold values show the best score (i.e., highest correlations or lowest absolute bias) among the "raw," "CR" and "MCF" solutions.

main issues; (1) the amount of missing entries in the observed dataset (Champagne et al., 2023); (2) the relatively small amount of variance beyond the diurnal and seasonal cycles; (3) the large time and spatial heterogeneities in the sampling.

To overcome some of the above issues, a *k*-means cluster analysis is applied to unfiltered diurnal LCF variations (i.e., variations within 1 day) (Figure 5). The clustering enables classifying all days at all available stations into basic diurnal types (DTs, see section 3.3), portraying typical variations of low cloud cover relative to the mean diurnal cycle, which usually peaks in late night and morning and decreases during the afternoon (Champagne et al., 2023; Dommo et al., 2022). The methodology, detailed in Figure 5, allows the optimization of the available data by following two different paths: (1) Using first the small set of complete daily records to define the DTs as centroids of the clusters of diurnal 3-hourly LCF (upper part of Figure 5) and (2) then projecting the remaining incomplete days (and ERA5), sampling at least the LCF around its usual highest and lowest daily intensity (lower part of Figure 5). This way, DTs can be defined meaningfully on 63% of the 234,416 "day-stations" despite the rather incomplete record. This approach is similar to the one performed on direct normalized irradiance by Philippon et al. (2019) and also allows a cross-scale analysis, since all variations from the diurnal to the interannual scales could be considered.

In order to determine the optimal number of clusters, the *k*-means clustering was repeated with 1000 replicates for each *k* from 2 to 10. The "classifiability" index (Michelangeli et al., 1995) shows a clear peak near the theoretical maximum of 1 for $k = 2$–3, then drops (not shown). The "Gap" index (Tibshirani et al., 2001) shows a maximum at $k = 10$, but a large increase between successive values of *k* is limited to the transition between

FIGURE 3 (a–f) Mean monthly low-level cloud cover fraction (LCF) (in oktas) in ERA5 corrected with convective rainfall $\geq$0.1 mm·h^{-1} (shading) and observations (dots) from 3-hourly data (1971–2019). The observations use LCF for cloud genus 4 to 8 only (LCF is set to zero when other cloud genera occur). ERA5 monthly means are computed for all available entries, while observed ones are shown as soon as at least 100 observations are available for each month in 1971–2019. (g–l) Correlations between observed and ERA5 interannual monthly mean anomalies (only for the 26 homogenized stations). Upward/downward triangles indicate positive/negative correlations and black triangles indicate significant positive correlations at the one-sided 95% level according to a random-phase test (Ebisuzaki, 1997; Janicot et al., 1996). [Colour figure can be viewed at wileyonlinelibrary.com]

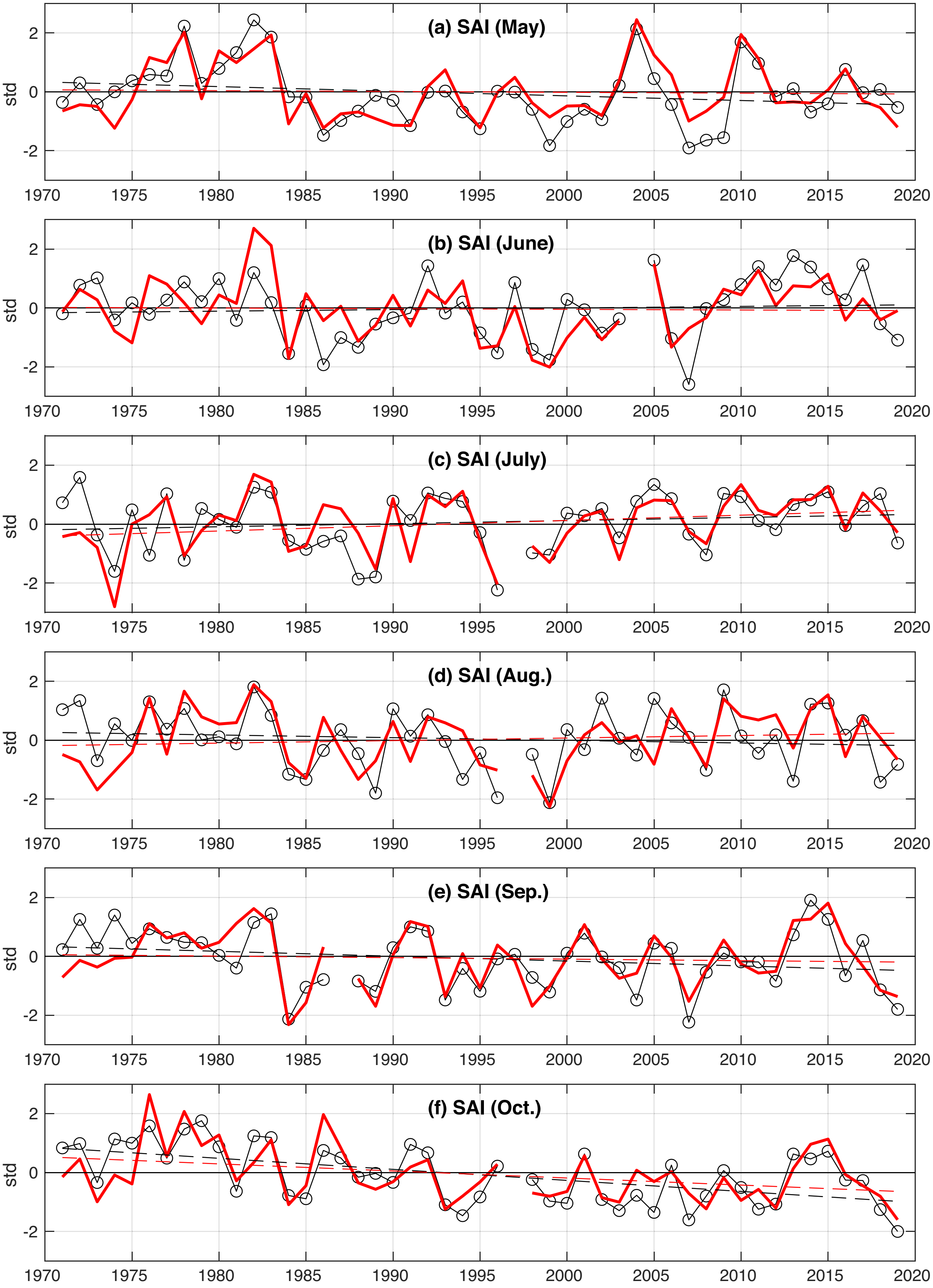

FIGURE 4 Legend on next page.

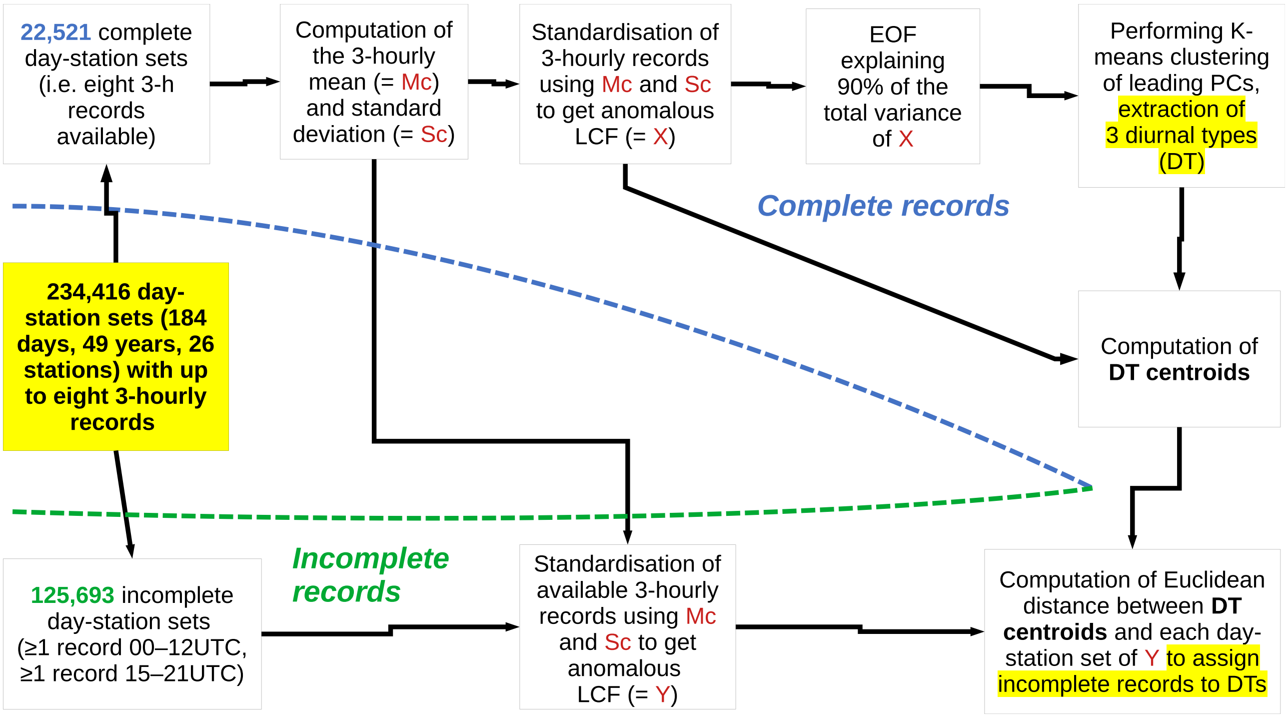

FIGURE 5 Flowchart of the methodological steps from the initial database of May–October 3-hourly low cloud fraction observed at the 26 homogenized stations to its clustering into three diurnal types (DTs) (starting and ending steps are underlined in yellow). The 3-hourly ERA5 LCF grid-points co-located with the 26 stations (prefiltered using the convective rainfall as explained in section 3.1) have been initially debiased versus Mc and then follow the "incomplete records" route [Colour figure can be viewed at wileyonlinelibrary.com]

$k = 2$ and $k = 3$ (not shown). The solution $k = 3$ is retained for the following analyses.

3.3 | Mean characteristics of the three types of LCF diurnal cycles

Figure 6 shows the average of raw LCF (Figure 6a,c,e) and the corresponding average distribution of LCG (Figure 6b,d,f) for the three DTs. DT#1 (Figure 6a) is less cloudy than the mean all through the day (<2 oktas) and corresponds broadly to the "bright" type identified by Philippon et al. (2019). It is referred to as the "clear" DT. DT#2 (Figure 6c) shows larger LCF than the mean during the late night and morning, and clearing during the afternoon. It is referred to as the "clear afternoon" DT. DT#3 (Figure 6e) shows the cloudiest conditions all along the day (>6 oktas) and is referred to as the "cloudy" DT.

It is striking that "clear" days are rarely cloudfree (Figure 6b). There are still scattered low clouds, which are mostly cumuliform (cumulonimbus with or without anvils; LCG#3 and #9). Stratocumulus is not absent at night but tend to be replaced by cumulus (LCG#1 and #2) during the afternoon. The "clear afternoon" DT (Figure 6d) shows both a transition from stratocumulus stricto-sensu (LCG#4 and #5) during the night to "small" and "bigger" cumulus, then to cumulonimbus with anvils thereafter (Figure 6d). Thus, this DT may be interpreted as a development of convection during the day, breaking at least partly the stratiform cloud deck. Lastly DT#3 mostly shows an increased frequency of stratocumulus plus cumulus (cloud genus 8) during the day (Figure 6f). However the clearing initiated during these days is too weak to lead to convection and a

FIGURE 4 Standardized anomaly index (SAI) of the interannual variations of monthly LCF of the "Gabonese and Congolese" stations defined in Figure 3g. The black + circle curve is the observed LCF while the red curve shows ERA5 LCF corrected with convective rainfall ≥ 0.1 mm·h^{-1}. The SAI used the same mask as in the observed LCF. Years are not shown when more than 50% of the stations are missing. The linear trends for observed LCF and ERA5 LCF corrected with convective rainfall ≥ 0.1 mm·h^{-1} are added as black and red dashed lines, respectively [Colour figure can be viewed at wileyonlinelibrary.com]

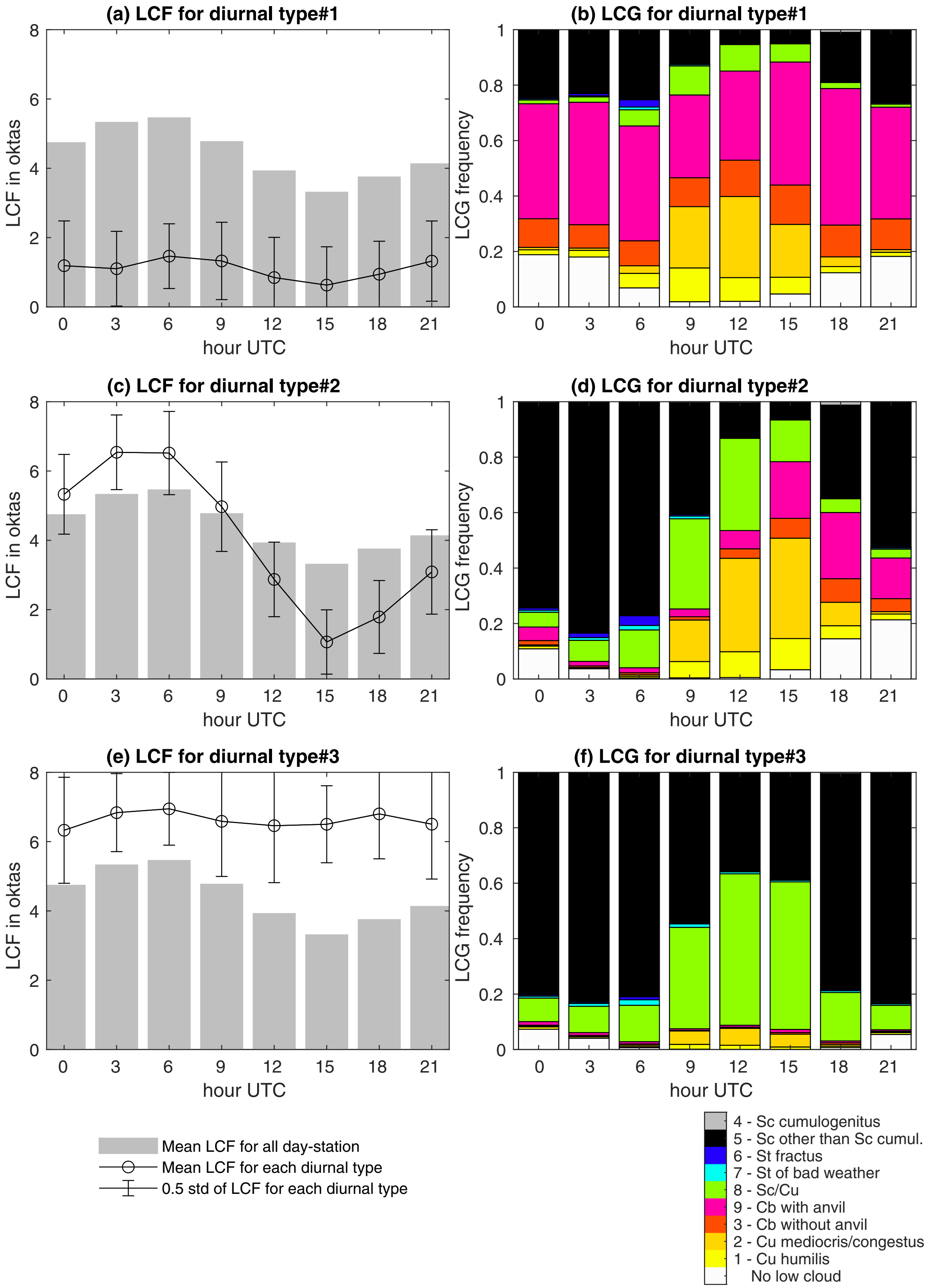

FIGURE 6 (a, c, e) Mean (May–October) low-level cloud fraction (LCF) (in oktas) averaged across the 22,521 station-days with eight available 3-hourly slots (grey bars). The mean LCF and ±0.5 standard deviations for the diurnal types (a) #1, (c) #2 and (e) #3 are superimposed as full lines with circles and vertical bars. (b, d, f) Relative frequency of the nine low-level cloud genus (+ no low cloud) (LCG) across the same 22,521 station-days for the diurnal types (b) #1, (d) #2 and (f) #3 [Colour figure can be viewed at wileyonlinelibrary.com] total clearing of the stratiform cloud deck as in DT#2 (Figure 6c,d). Nonetheless, the usual diurnal modulation of the stratiform cloud deck is pretty similar in both DT#2 (Figure 6d) and #3 (Figure 6f), from dominant LCG genus #5 at night to fragmented stratocumulus, then to small or bigger cumulus or even cumulonimbus. Note that the DTs obtained using the incomplete 148,214 day-stations (Figure 5) are very similar to Figure 6 (not shown), but that the frequency of the "clear" type increases from 24.7% to 35.5% while the one of the "cloudy" type decreases from 43.3% to 31.5% (the frequency of the "clear afternoon" type is almost unchanged at 33%). This is due to the fact that a lot of incomplete "station-days" are outside the cloudiest sector, i.e. most of Gabon and southwestern RC (Figure 3a–f).

Note that 54% of all available 148,214 observed "station-days" (Figure 5) are classified in the same DTs in ERA5 and observations. This fraction is satisfactory regarding the large amount of noise among neighbouring stations. ERA5 produces too many "clear afternoon" days (44% vs. 33% in observations). The worst errors (i.e., "clear" DTs in observations vs. "cloudy" DT in ERA5 and vice versa) account for only ∼6% of the daily cases, while ∼19% are expected by chance. In the following analyses, observed DTs are used, but using ERA5 DTs leads to similar results.

Figure 7 shows the monthly frequencies of the three DTs across the 26 stations. The "clear" DT is rather frequent (∼60%) east of 14°E and north of 2°–3°N all along the season while it is rather rare over most of Gabon and SW of RC (<20%), and conversely for the "cloudy" DT. This is consistent with previous analyses (Dommo et al., 2018; Philippon et al., 2016, 2019). The "clear afternoon" DT shows less spatial variations than the "clear" one. Figures 6 and 7 suggest overall that afternoon clearing may be interpreted both as a temporal and spatial transition around the complete overcast conditions, peaking mostly in July and August and covering most of Gabon and southwestern RC in that season (∼2°N–6°S, W of 14°E), referred to as the "core" area hereafter. It gives way to less cloudy conditions, mostly in the form of afternoon clearing, both around the core area and during the transition months of June and September. Lastly, clear days (or with convective activity) prevail further away from the core area or the cloudiest season (JJAS), that is, in May and October, and north of 2°N and east of 14°E during all months. Note also that the starting (May–June) and ending (September–October) stages of the cloudy season are not perfectly symmetrical. There is still a large frequency of the "cloudy" DT over western Gabon and the extreme southwest of RC in September, and even October at coastal stations (Figure 7), while the start of the cloudy season in June is more abrupt and spatially uniform over the cloudiest area (Figure 7).

3.4 | Interannual variations of the low cloud fraction

In this subsection, we analyse the space–time interannual variations of low-level cloud cover during the core of the cloudy season of JJAS (Figures 3 and 7), as in Champagne et al. (2023) and Camberlin et al. (2023). Classical EOF analysis is applied to the frequencies of the three DTs. We have to deal with (1) the relatively large number of remaining missing entries (=37%) and (2) the fact that these missing entries may be located at different periods of the JJAS season across the years and stations. So computing directly the relative frequency of the available three DTs in JJAS may be biased, for example if the available entries for one station and one year are concentrated in June (usually less stratiform clouds than on average during JJAS) or July (usually more low-level clouds). We thus used a preprocessing to compute JJAS anomalies for each station and each diurnal type. A 11-day running window is first used on MJJASO to compute the running relative frequencies of the three diurnal types at each station and on each year, as soon as at least 50% of the 11 days are available. Note that using a 21- or a 31-day running window leads to almost the same results (not shown). We prefer the shortest length to better handle intraseasonal variations. The climatological mean is then computed across the years for each station and each diurnal type from these low-pass filtered frequencies. The anomalies relative to this climatological mean (i.e., (obs-clim)/clim) are computed. We then cut out each season to retain the JJAS temporal averages only, and any season-station having less than 50% of available days is set to a missing entry. The amount of missing entries in this final matrix is slightly reduced to 29%.

An EOF (Figure 8) is then applied to the standardized JJAS mean anomalies of this matrix including 49 years of observations and the 78 DTs – stations (i.e., 3 DTs × 26 stations) as variables. The correlation matrix is computed on the available entries for each couple of DT – station. The three DTs of ERA5 are processed exactly in the same way, except that there are no missing entries. Note that using the observed missing mask on ERA5 time series leads to almost the same results (not shown). Overall, the first EOF mode mostly opposes the JJAS frequencies of the clear DT (Figure 8a) on one hand, and those of the cloudy DT (Figure 8c) on the other hand, with a larger coherence (i.e., less spatial variations) for the latter one. It suggests that the main interannual signal is mostly discriminated on whether the stratiform cloud cover clears or not during the afternoon, thus opposing anomalously clear seasons, that is, more "clear" and "clear afternoon" DTs than usual, to anomalously cloudy ones. The spatial pattern of the loadings and the temporal variability of the

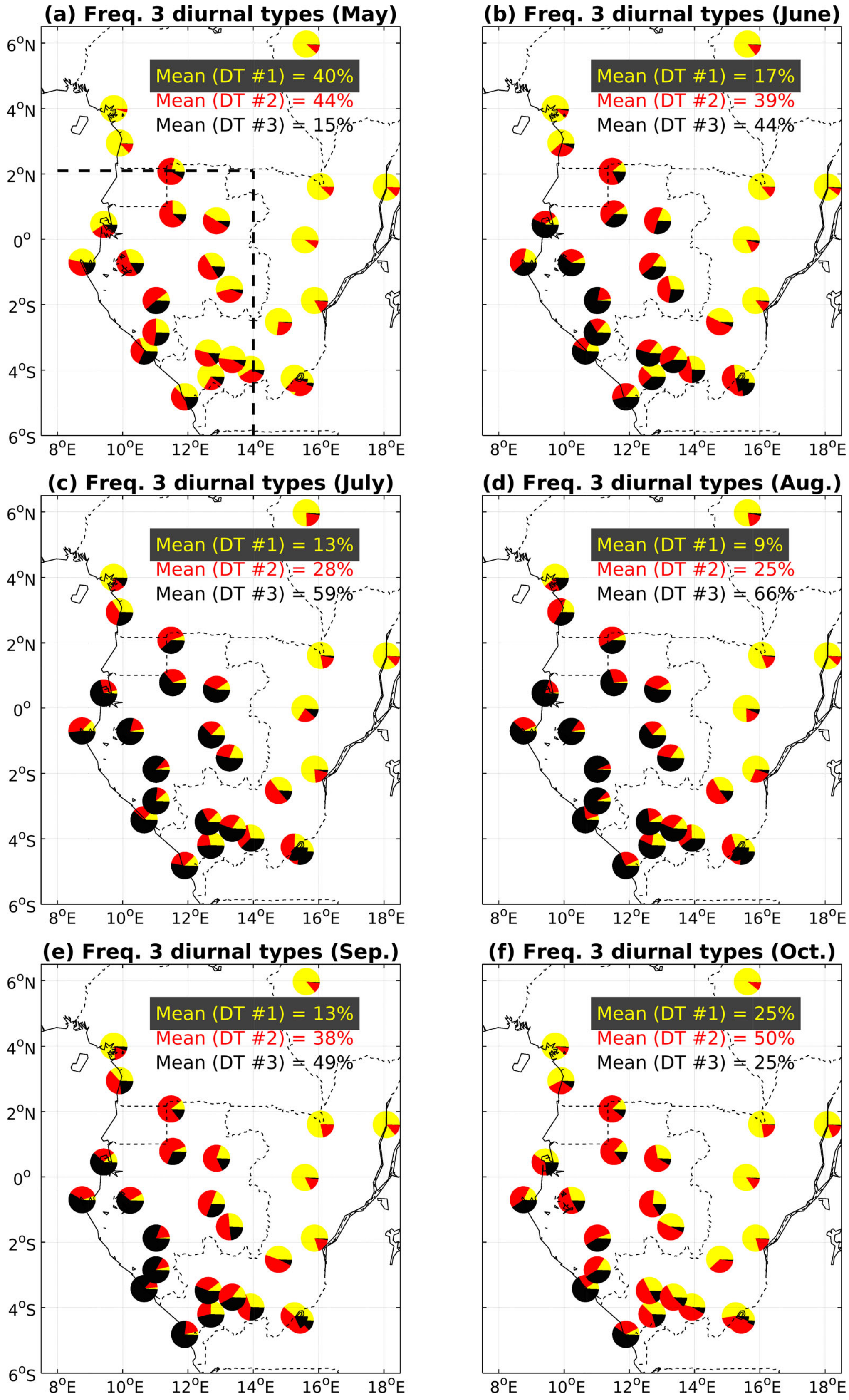

FIGURE 7 Relative mean monthly frequency of the three diurnal types of the stratiform cloud cover (yellow = diurnal type #1; red = diurnal type #2; black = diurnal type #3 defined in Figure 6). The values show the mean frequency of the three diurnal types for the 16 stations enclosed by the dashed line on panel (a) [Colour figure can be viewed at wileyonlinelibrary.com]

leading mode of the three diurnal types in ERA5 (Figure 8d–f,h) are consistent with the observed ones: the spatial correlations between observed (Figure 8a–c) and ERA5 patterns (Figure 8d–f) are >0.49 and the temporal correlation between the corresponding PC#1 (Figure 8h) is 0.77. However, as expected from a gridded product, the spatial coherence is stronger in ERA5 than in observations (explained variance by the leading EOF mode of the WEA low-level cloud cover equals 74% vs. 45% in observations) and the "clear afternoon" DT is more tightly linked to the "clear" DT than in observations. There are also subtle differences such as the strongly negative ERA5 loadings of the "clear afternoon" DT over SW RC (Figure 8e) which are not observed (Figure 8b). Figure 8g shows that the eastern edge of the covariant LCF area of the leading EOF mode near 15°E fits almost perfectly with the mean LCF (Figure 3), suggesting that factors driving the mean space–time annual cycle may also operate at interannual time scale. Figure 8g shows that LCF in the Atlantic north of the equatorial upwelling is also tightly linked to the leading EOF mode of the WEA low-level cloud cover, while it is not so true just off the Gabon and RC coasts. In the following, we use the observed time series of the leading EOF mode of the three DTs (i.e., PC#1 in Figure 8h hereafter simply referred to as "PC#1") to diagnose the relationships between interannual variations of stratiform clouds and various regional to large-scale potential drivers.

4 | DRIVERS OF THE INTERANNUAL VARIATIONS OF THE STRATIFORM CLOUD DECK

4.1 | Climatological atmospheric circulation

We first document the climatological JJAS winds, temperatures and relative humidities on two altitude-longitude and altitude-latitude sections over WEA (Figure 9). On the equatorial zonal plane (Figure 9a,c), there is a clear opposition between the Atlantic Ocean, where subsidence extends over the whole troposphere, with a clear thermal inversion centred near 900 hPa at low levels, and the Congo Basin with weak and diffuse ascending motion. This E-W dipole is associated with a vertical shear across the Congo Basin with low-level westerlies peaking near 12°–16°E around 900 hPa, and middle and upper easterlies above 825 hPa and peaking around 700 hPa (i.e., near the level of the African Easterly Jet; Nicholson & Grist, 2003), consistent with the westward thermal gradient (Figure 9c), and above 300 hPa (i.e., the tropical Easterly Jet) (Figure 9a) At low levels, relatively moist air is located over the Atlantic ocean and it is interesting to note a maximum relative humidity ≥95% on the windward slopes of WEA where shallow ascent, probably due to the interaction between topography and the low-level westerlies, occurs (Figure 9c). A foehn effect and a localized decrease of low-level relative humidity leeward of the main topographical WEA features (Figure 1) are also observed (Figure 9c). Above the boundary layer, between 850 and 750 hPa, the air is relatively drier and warmer over the Congo Basin east of 16°–18°E than over WEA (Figure 9c). Note that the absolute amount of moisture in the middle levels is, however, higher over the Congo Basin than over the Atlantic Ocean and WEA (not shown).

In the meridional plane (Figure 9b,d), there is also a clear dipolar structure between subsidence over the equatorial and southern parts and the deep convection, moistening the middle and upper troposphere (Figure 9d), associated with the African monsoon centred around 5°–7°N, just over the Adamaoua mountains in Cameroon. In the low levels, the southerlies extend farther to the north, consistent with the well-known tilted structure of the continental ITCZ over Africa and the deeper northward penetration of the low-level monsoon flow (Nicholson & Grist, 2003). Northerlies associated with the southern Hadley cell occur above ~650 hPa south of the ITCZ (Figure 9b).

4.2 | A tropical-scale view

Overall, positive anomalies of PC#1 (i.e., years with a more frequent cloudy type and less frequent clear and clear afternoon types; Figure 8h) tend to be first related to an anomalously cold equatorial and southern Atlantic and then to warm ENSO events (Figure 10). Local anomalously cold SSTs over the equatorial and southern Atlantic increase vertical stability and thus lead to more stratiform clouds than usual, locally and downstream, in association with the advection of the cool Atlantic air by the basic low-level flow (Figure 9a). The teleconnection to ENSO implies a modulation of the large-scale, zonal overturning equatorial cells, that is, associating anomalous subsidence over WEA during warm ENSO events. Concomitant anomalous warm anomalies over the Indian Ocean potentially increase the west–east thermal gradient with the equatorial Atlantic and thus increase the low-level westerlies (Figure 9a). These correlations only marginally change when the linear trend is removed from 2-m temperatures and PC#1 suggesting they are not strongly impacted by global warming trends (not shown). Significant but weaker correlations are also found over

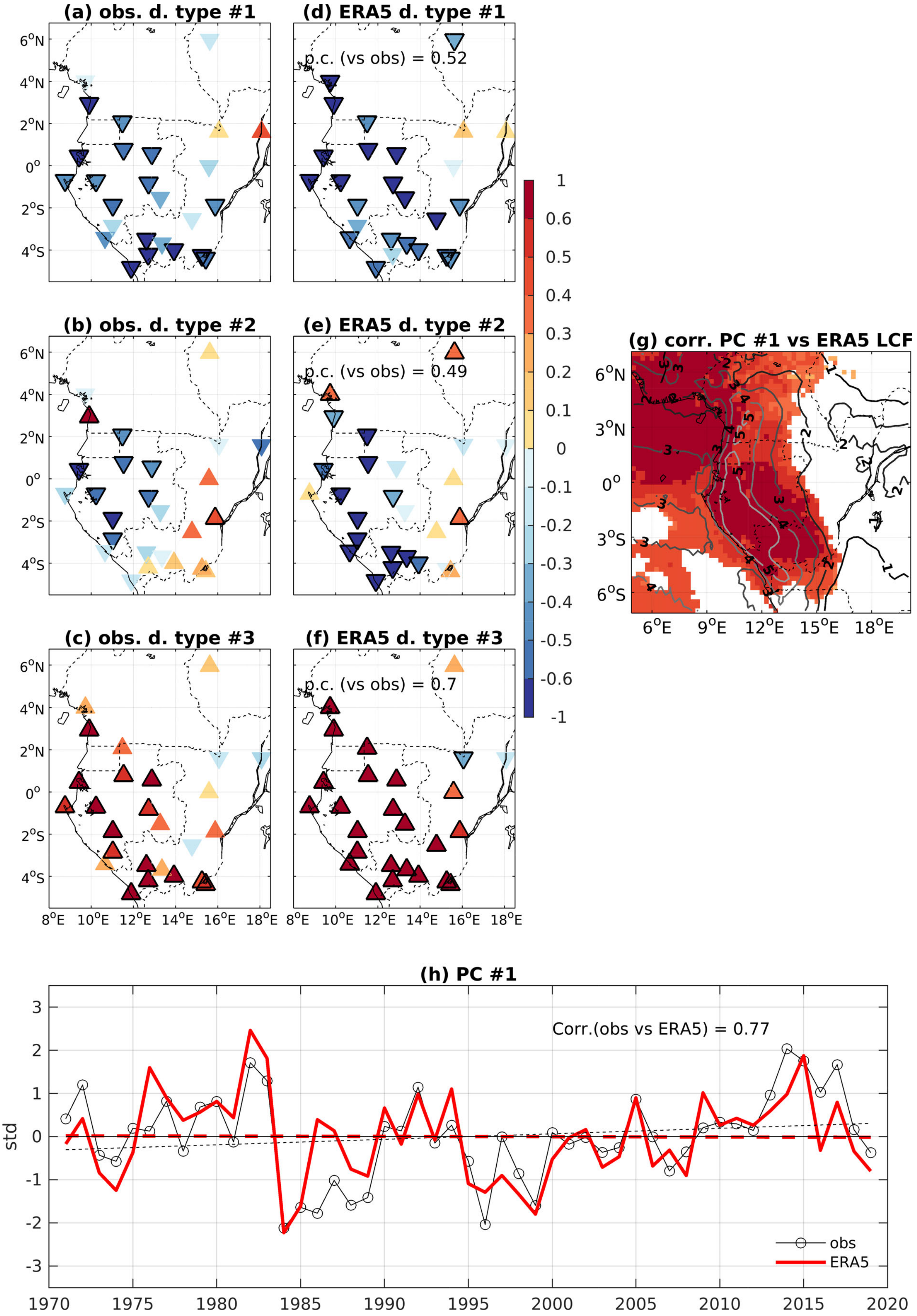

FIGURE 8 Legend on next page.

land areas. Weak positive correlations are located over East Africa and over a broad area from the northern Congo Basin to Lake Chad, when the linear trend is removed (not shown). Higher land temperatures over these areas combined with lower temperatures over the South Atlantic are likely to increase the low-level westerlies and or southerlies over WEA.

Figure 11 shows full and partial correlations between PC#1 and three SST indices for JJAS (southern and equatorial Atlantic [SAT]: 10°W–10°E, 10°S–Eq; Benguela area [BEN] 10°E to the coast, 15°–7°S; Niño 3.4 [N34]: 170°–120°W, 5°S–5°N). SAT is obviously strongly related to BEN ($r = 0.82$, significant at the 99% level) since they belong to the same oceanic system and are close to each others, while both Atlantic SST indices share some common variance with N34 ($r = -0.38$, significant at the 99% level for SAT and $r = -0.27$ for BEN). SAT and BEN are strongly related to PC#1 in the expected way (i.e., more stratiform clouds when SAT and BEN are anomalously cold and vice versa) and these relationships slightly increase, especially for BEN, when the long-term warming (i.e., +0.39 K for SAT [$p = 0.91$] and +0.93 K [$p > 0.99$] for BEN in JJAS from 1971 to 2019) is removed (Figure 11a). The correlations between PC#1 and both SAT and BEN just slightly decrease when the linear influence of N34 is removed (Figure 11a). It contrasts with N34, whose positive correlation with PC#1 ($r = 0.40$, significant at the 99% level) decreases when the linear influence of SAT is removed (Figure 11a). It suggests that the ENSO impact on the stratiform cloud over WEA is merely due to a covariation between SAT and N34. However, correlating May SST with PC#1 shows highest correlations with BEN and then N34 (Figure 11b). In particular, N34 remains positively correlated to PC#1, even when the linear influence of SAT is removed (Figure 11b). These results suggest a delayed influence of ENSO upon the interannual variations of the stratiform cloud over WEA, while the relationships with the southeastern and equatorial Atlantic are probably more direct and likely involve ocean–atmosphere coupling over the whole upwelling system. Precursor signals in SST may be sought on the southeastern Atlantic rather than on the equatorial Atlantic area.

Correlations between PC#1 and rainfall (Figure 12) show again some consistent large-scale signals. Positive anomalies of PC#1 (i.e., more cloudy days) are locally related to less rainfall than usual over WEA, which is expected since low-level clouds are not rain-bearing and may help suppress deeper clouds by reducing surface heating. However, this meridional signal extends over a much larger area to the west across the Atlantic Ocean, reaching central and northern Amazonia (Figure 12), where the negative rainfall anomalies are associated with warm anomalies (Figure 10). As for temperatures, removing linear trend from rainfall does not really change the pattern and amplitude of correlations (not shown). Lastly, a weak ENSO teleconnection pattern appears in rainfall correlations (Figure 12), fully consistent with what has been observed with 2-m temperatures (Figure 10). Note that no significant positive correlations appear over either the Sudanian/Sahelian belts or equatorial East Africa and the eastern part of the Congo basin, suggesting that convection over these areas does not drive subsidence over WEA.

4.3 | Atmospheric and oceanic controls on the low-level cloud cover in WEA

We further use PC#1 (Figure 8h) to diagnose the relationships between the stratiform cloud cover and regional-scale (i.e., 0°–25°E, 12.5°S–12.5°N) atmospheric variables extracted from ERA5. Figure 13 shows the synchronous correlations between PC#1, SAT, N34 SST indices and various atmospheric variables between 950 and 700 hPa. Figure 14 shows the synchronous correlations between PC#1 (a, b), SAT (c, d) and N34 (e, f) and atmospheric variables averaged on the same two cross-sections as used in Figure 9. The correlations in Figures 13b,e,h and 14c,d are computed with -SAT (instead of SAT), such that all maps are easily compared to Figure 8h.

As expected from theory, an increased LTS is associated with an increased low-level cloud cover, as observed for other stratiform cloud areas (Figure 13a) (Klein & Hartmann, 1993; Klein et al., 1995; Norris, 1998a, 1998b; Zhang et al., 2009). The significant correlations associating anomalously low temperatures and anomalously cloudy JJAS seasons are restricted mostly to below 900 hPa over the Atlantic Ocean and the adjacent WEA coast (Figures 13a and 14a,b). There is a clear shallow

FIGURE 8 Leading JJAS EOF mode of (a–c) observed and (d–f) ERA5 anomalous frequencies of the three diurnal types of the stratiform cloud cover defined in Figure 6 (shown as loading, i.e., correlation between the leading principal component (panel (h)) and the original data; black contour indicates significant correlations at the two-sided 95% level according to a random-phase test (Ebisuzaki, 1997; Janicot et al., 1996). "p.c." on panels (d–f) are pattern correlations between observed and ERA5 loadings. Panel (g) represents the correlations (shades) between PC#1 and JJAS ERA5 LCF filtered with convective rainfall (see methods) superimposed on the mean filtered ERA5 LCF in oktas (contours) [Colour figure can be viewed at wileyonlinelibrary.com]

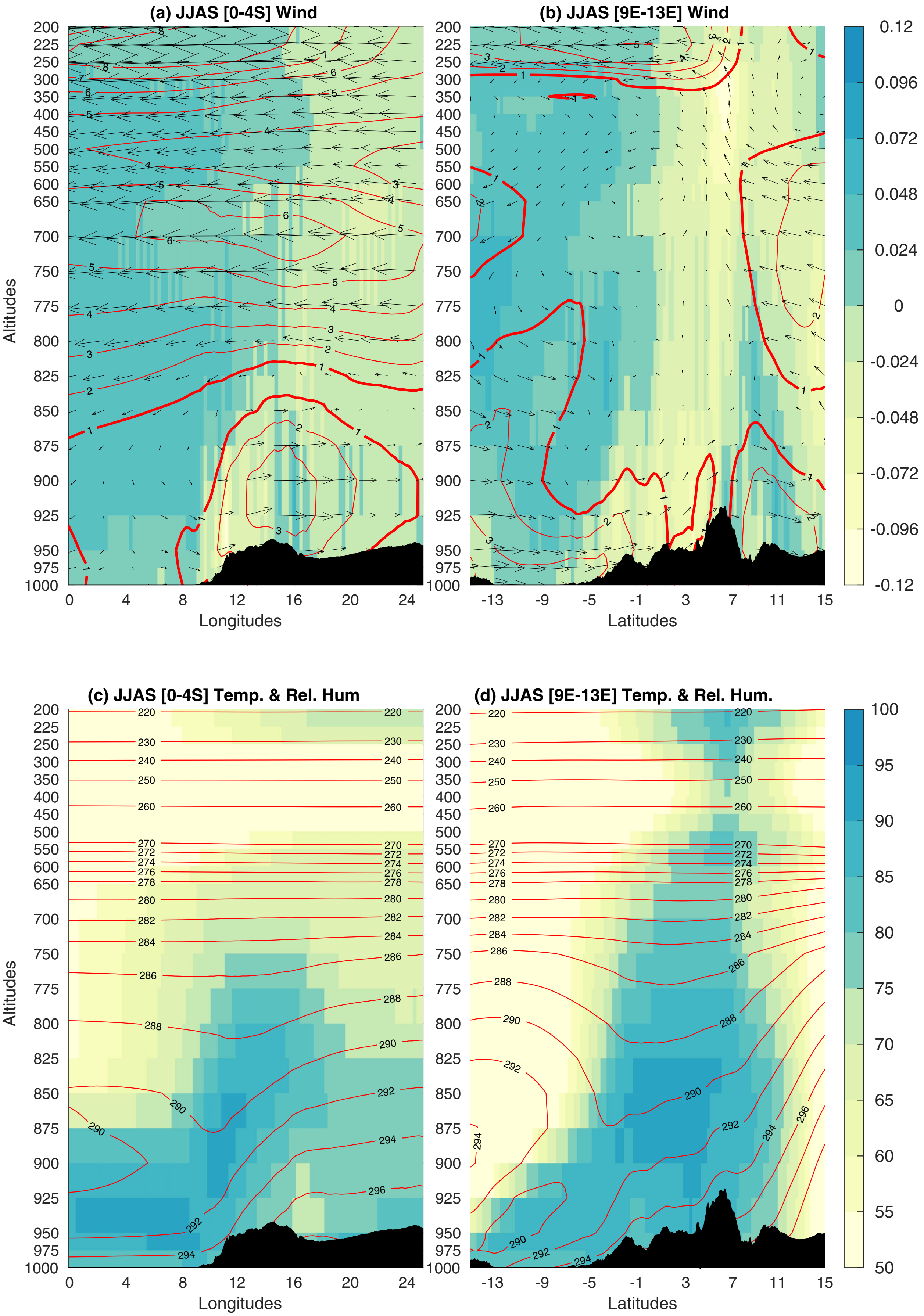

FIGURE 9 Legend on next page.

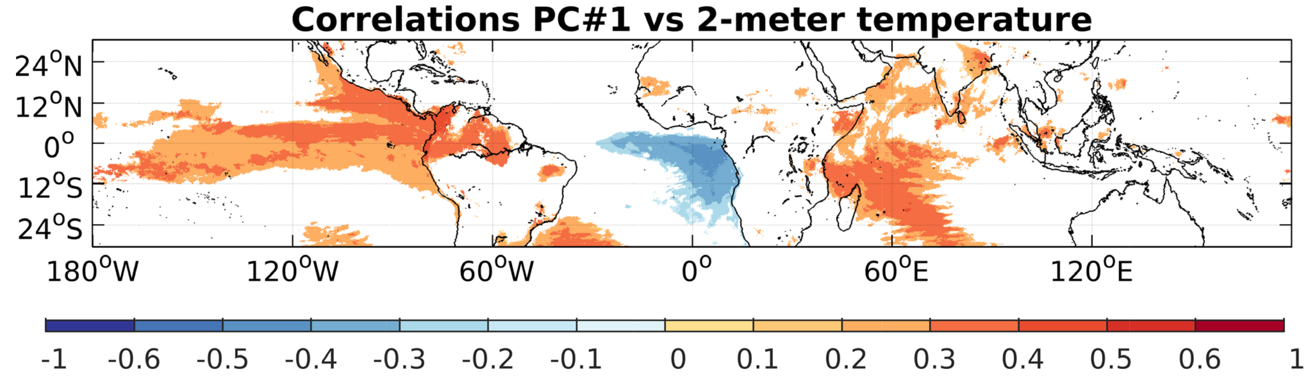

FIGURE 10 Correlations between the observed JJAS PC#1 of anomalous frequencies of the three diurnal types of stratiform cloud cover (Figure 8h) versus 2-m temperature (from ERA5). Nonsignificant correlations at the two-sided 95% level according to a random-phase test (Ebizusaki, 1997; Janicot et al., 1996) are masked out [Colour figure can be viewed at wileyonlinelibrary.com]

vertical out-of-phase relationship, mostly on the meridional plane (Figure 14b), between anomalously cloudy conditions in WEA on one hand and anomalous southerlies at 950 hPa, veering to anomalous southwesterlies over Gabon and northern RC (Figures 13d and 14b), and anomalous northerlies at 850 hPa (Figures 13d and 14b) over the Bight of Bonny and WEA, on the other hand. This shallow and localized circulation is seen as a counterclockwise pattern in the latitude–altitude plane between roughly 7°S and 7°N (Figure 14b). This is consistent with the boreal spring LLAC model (Leduc-Leballeur et al., 2013; Meynadier et al., 2016), with enhanced LLAC increasing subsidence and low-level cloud around the equatorial Atlantic and adjacent WEA. We can also notice that the anomalously moist air, mostly below 950 hPa, over the whole equatorial Atlantic and windward areas, including WEA (Figures 13a and 14a), is also associated with more cloudy conditions over WEA. There is also a positive RH anomaly in the middle troposphere between 900 and 750 hPa between 5°S and 7°N over WEA (Figure 14b).

Relationships on the zonal plane are less obvious. Anomalously cloudy conditions are associated with anomalous subsidence around 12°E, combined with anomalous divergence below 875 hPa as a result of anomalous westerlies over the continent and anomalous easterlies over the equatorial Atlantic and coastal area of WEA (Figure 14a). In the middle troposphere, the correlations suggest increased easterlies especially west of 12°E around 750 hPa when PC#1 is positive (Figures 13g and 14a). Above 700 hPa, the wind signals are weak, except for the anomalous subsidence already noticed above 12°E and weak warm anomalies in the middle and upper troposphere in years of anomalously cloudy conditions in WEA (Figure 14a). Over the ocean, there is no clear vertical out-of-phase wind pattern and most of the significant wind anomalies are easterlies (Figure 14a). This analysis suggests that anomalously strong easterlies at 700 hPa and above in conjunction with weak warm anomalies (Figures 13g and 14a,b), together with the colder boundary layer, increase LTS, and thus the stratiform clouds.

Both SAT (Figure 13b,e,h) and N34 (Figure 13c,f,i) synchronous correlations project more or less on the patterns of the correlations with PC#1 (Figure 13a,d,g). Overall, and as expected from raw correlations between PC#1 and SST indices (Figure 11), the spatial agreement is better with SAT than with N34, especially for the shallow meridional cell (Figures 13a,b,d,e and 14b,d). It is expected that a stronger equatorial cold tongue than usual is able to drive an enhanced LLAC, through, at least, strengthened meridional thermal and pressure gradients, but may be also impacted through the increased surface wind speed, which intensifies the upward heat fluxes and cools down the SST. About SAT, we can notice that the positive relationships with temperature are far

FIGURE 9 (a) Longitude-altitude cross-section of climatological JJAS averages (1971–2019) of of ERA5 zonal and vertical components of the wind (arrows) from 0 to 25°E. Vertical winds (in Pa·s^{-1}) are also displayed as shadings, and the magnitude of the zonal winds (in m·s^{-1} with a contour interval of 1 m·s^{-1}) is displayed as red lines. All winds are averaged over 0°–4°S. (b) Same as (a) for a latitude-altitude cross-section from 15°S to 15°N, averaged over 9°–13°E, except that arrows and red lines display meridional instead of zonal winds. Panels (c, d) show the same longitude-altitude and latitude-altitude JJAS climatological cross-sections for temperature (in K with a contour interval of 5 K) as red lines and the relative humidity (in %) as shadings [Colour figure can be viewed at wileyonlinelibrary.com]

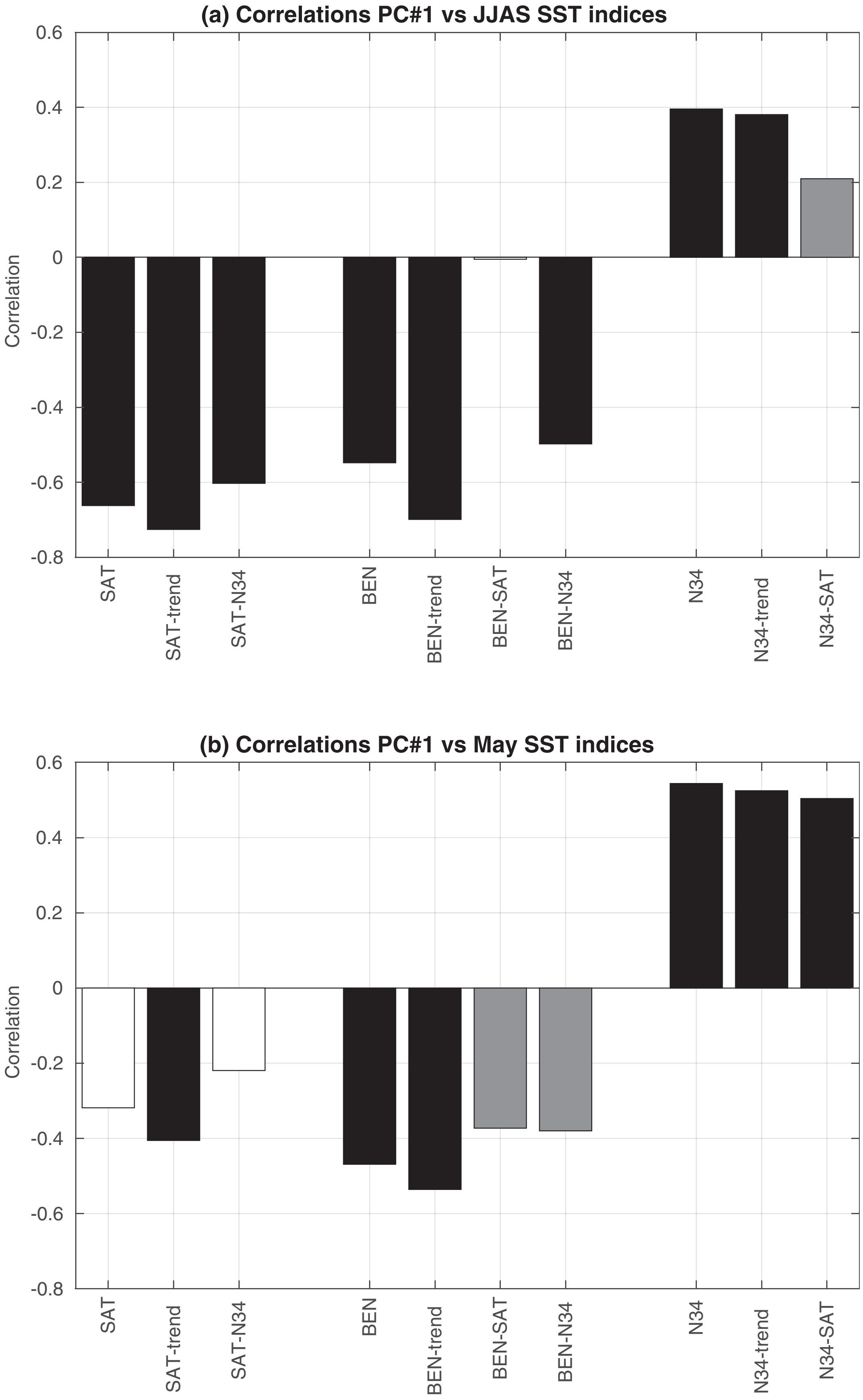

FIGURE 11 Legend on next page.

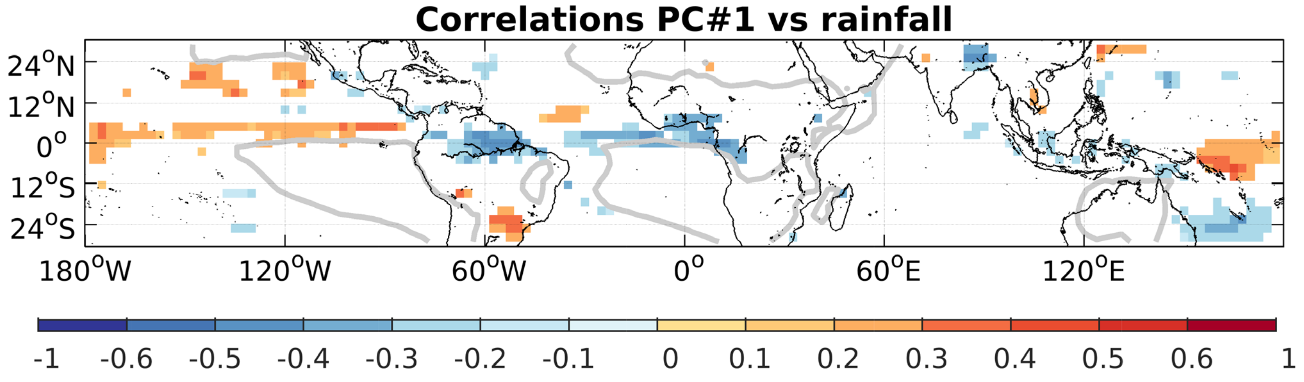

FIGURE 12 As Figure 10 but versus rainfall (from GPCP v2.3 on 1979–2019). Areas receiving less than 50 mm in JJAS in mean are masked out and delineated by a grey line [Colour figure can be viewed at wileyonlinelibrary.com]

larger and extend to 850 hPa, mostly north and eastward of the equatorial upwelling (Figure 13b,e). Another difference between correlations with PC#1 and those with SAT is a stronger relationship with low-level westerlies, which are increased over the Congo Basin when SAT is anomalously cold (Figure 14c).

On the contrary, N34 has a better agreement with PC#1 correlations at and above 700 hPa, especially for wind (Figures 13i and 14e,f). In fact, anomalously warm N34 anomalies are associated with anomalous easterlies (or northeasterlies) over all the land areas at 850 and 700 hPa, as well as with weak warm anomalies (Figures 13f,i and 14e,f). Note that the weak easterly anomalies related to warm ENSO events observed in the lower troposphere over the WEA area (Figure 14e) may partly weaken the anomalous low-level westerlies over the Congo Basin associated with anomalously cold SAT (Figure 14c), thus decreasing the relationship with PC#1 over this area (Figure 14a). When the correlations are computed with May SAT and N34 (as in Figure 11b), the SAT pattern weakens while the N34 one strengthens, especially for the anomalous warm anomalies in the middle and upper troposphere related to warm ENSO events (not shown). The mid- to upper-tropospheric temperature signal is likely related to the tropic-wide warming (cooling) of the middle troposphere associated with warm (cold) ENSO events (Trenberth & Smith, 2006; Yulaeva & Wallace, 1994).

Finally, Figure 15 offers a view on the relationships between six atmospheric indices associated with interannual variations of the stratiform cloud cover over WEA (Figures 13 and 14) and SAT-N34 SST indices, matching some of the analyses for CMIP6 simulations by Camberlin et al. (2023). Note that the correlation values shown in Figure 15 are not very sensitive to the choice of the spatial windows. LTS, V1000 and V850 are tightly linked to each other ($r = -0.82$ between V1000 and V850, $r = -0.76$ between LTSwea and V850 and $r = 0.84$ between V1000 and LTS). The correlations with PC#1 only slightly decrease in amplitude when the linear influence of N34 is removed, but those with N34 strongly decrease when the linear influence of SAT is removed (Figure 15a–c). Overall, these results suggest a weak impact of ENSO on LTS and the meridional cell over the Bight of Bonny. It is also interesting to note that, even without the linear influence of SAT, the correlations between LTS-V1000-V850 and PC#1 decrease in amplitude but are still significant at the 99% level (Figure 15a–c), suggesting some purely atmospheric processes in play. The correlations with U950 (Figure 15d) are overall weaker, but exhibit broadly the same modulation (i.e., N34 impact is weak) except that removing the linear influence of SAT removes the (weak) positive correlation. This differs strongly for U700 and especially T700 (Figure 15f). For them, the correlations involving PC#1 decrease in amplitude, when the linear impact of N34 is removed. For T700, removing the linear impact of SAT strongly increase the positive correlation with PC#1 (Figure 15f). Considering May SST indices (as for Figure 11b) usually show larger (smaller) absolute

FIGURE 11 Full and partial correlation between the observed JJAS PC#1 of anomalous frequencies of the three diurnal types of stratiform cloud cover (Figure 8h) and three SST indices (SAT: 10°W–10°E, 10°S–Eq; BEN: 10°E to the coast, 15°–7°S; N34, 170°–120°W, 5°S–5°N) from ERA5. The correlations are computed with (a) JJAS and (b) May values of the SST indices, with and without linear trend ["-trend"] of all timeseries. The partial correlations ["-SAT" and "-N34"] are computed without the linear influence of SAT and N34, respectively. The grey (black) bars display significant correlations at the two-sided 90% (99%) level according to a random-phase test (Ebisuzaki, 1997; Janicot et al., 1996)

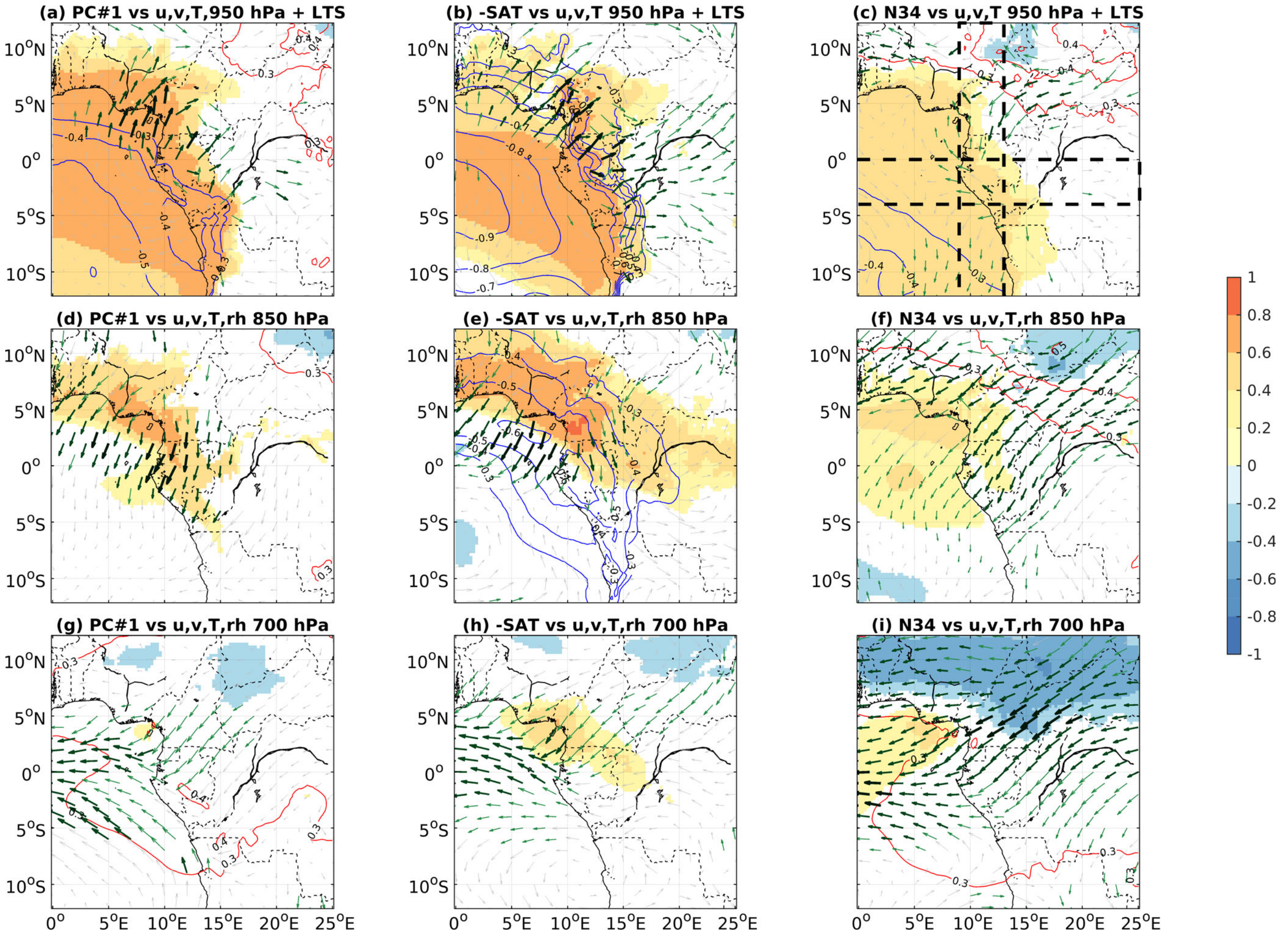

FIGURE 13 Correlations between the observed JJAS PC#1 of anomalous frequencies of the three diurnal types of stratiform cloud cover (Figure 8h) and (a) zonal and meridional component of the wind (vectors), temperature (contours) at 950 hPa, and lower-tropospheric stability (shadings); (d) zonal and meridional component of the wind (vectors), temperature (contours), and relative humidity (shadings) at 850 hPa; (g) zonal and meridional component of the wind (vectors), temperature (contours) and relative humidity (shadings) at 700 hPa; (b, e, h) same as (a, d, g) except for -SAT index; (c, f, i) same as (a, d, g) except for N34 index. For shadings, only significant correlations at the two-sided 95% level are shown. For temperature, a level of 0.3 corresponds roughly to the two-sided 95% level and negative (positive) correlations are shown as blue (red) lines below −0.3 (above 0.3) with a contour interval of 0.1. For winds, significant correlations at the two-sided 95% level with absolute amplitude below 0.4, between 0.4 and 0.6 and over 0.6 are displayed as light green, green, and dark green vectors (respectively) of increasing widths. The dashed lines in panel (c) delineate the longitudes and latitudes of the cross-sections shown in Figures 9 and 14 [Colour figure can be viewed at wileyonlinelibrary.com]

correlations for N34 (SAT) and using BEN index again shows larger correlations than SAT ones (not shown).

5 | DISCUSSION

This section discusses how the relationships between the interannual variations of PC#1 of JJAS stratiform cloud (Figure 8) and zonal and regional-scale oceano-atmospheric modes of variations revealed by Figures 9–15 15 could be integrated into interrelated physical mechanisms. At least, two complementary mechanisms are important to understand the interannual variations of stratiform clouds during JJAS: (i) a shallow meridional and regional-scale overturning, mostly involving the equatorial Atlantic Ocean and (ii) a zonal pattern (i.e., not necessarily a cell) involving a broader spatial scale of tropical atmospheric anomalies. Both mechanisms are strongly related to SST variations over the coastal and equatorial Atlantic, which were shown to be negatively correlated to stratiform cloud cover over WEA. Note that this relationship is not adequately reproduced by many coupled climate models from CMIP6 (Camberlin et al., 2023).

The meridional mechanism is detected here primarily from the opposite correlations between WEA stratiform

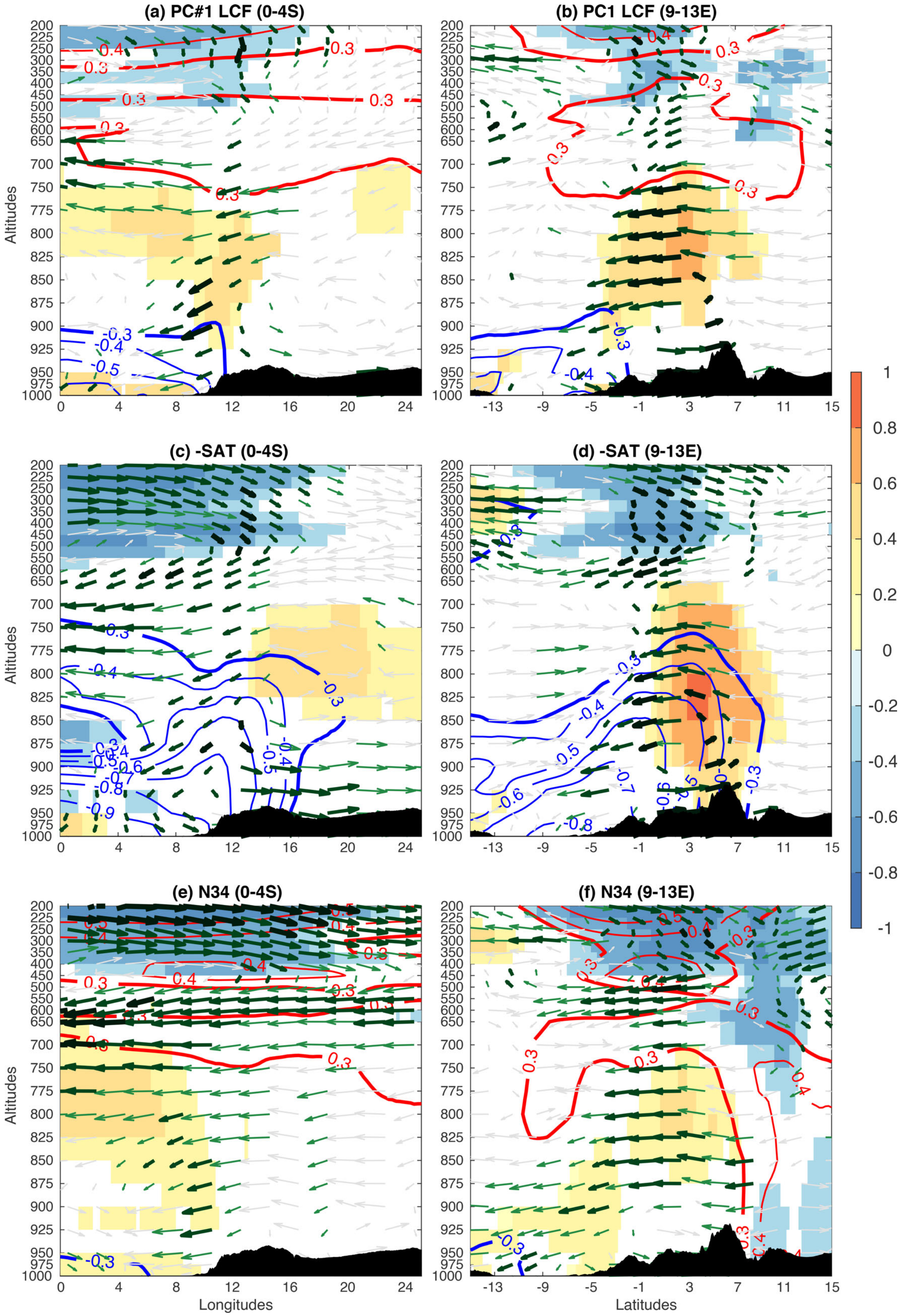

FIGURE 14 Legend on next page.

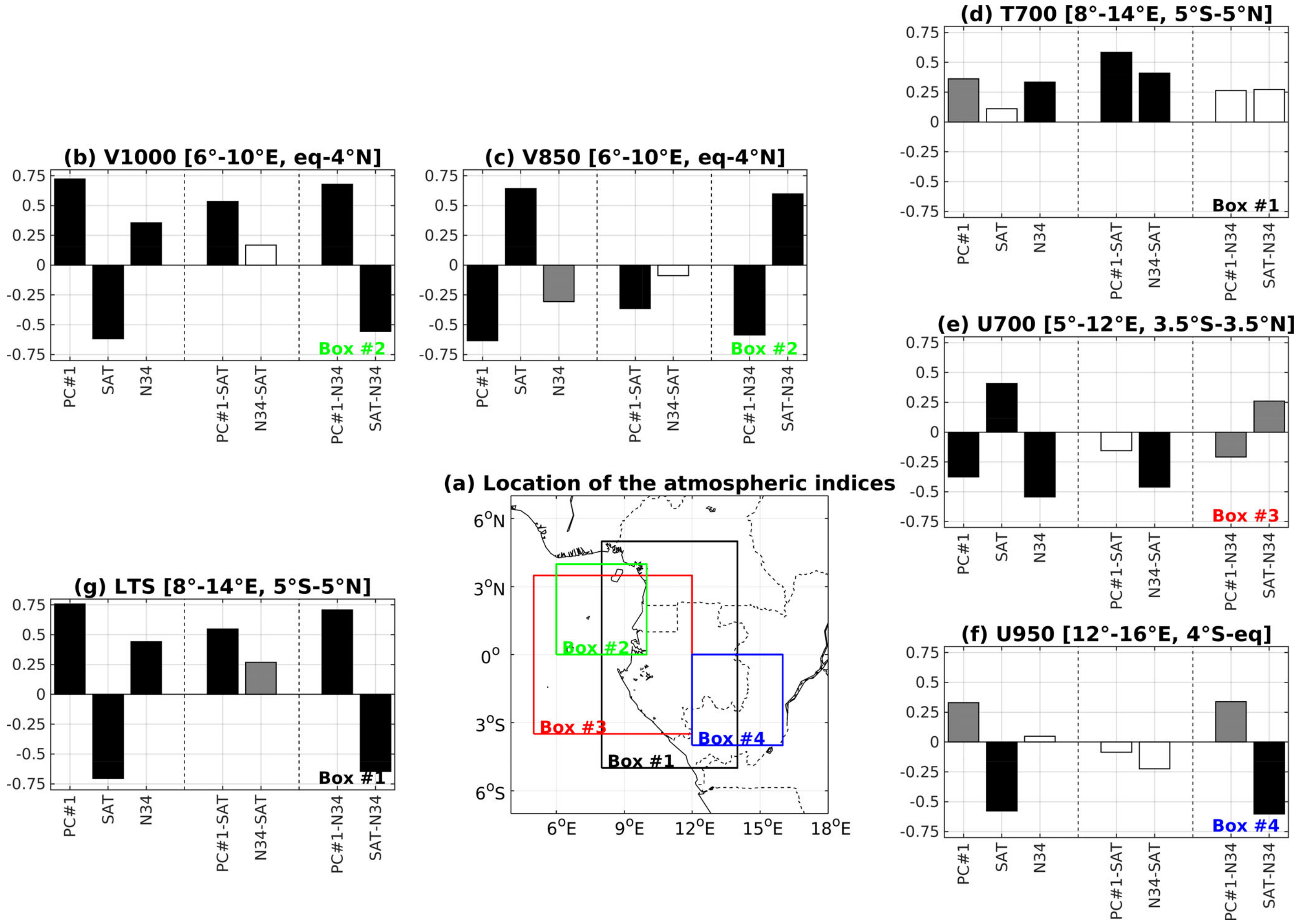
(d) T700 [8°-14°E, 5°S-5°N]

(b) V1000 [6°-10°E, eq-4°N]

(c) V850 [6°-10°E, eq-4°N]

(e) U700 [5°-12°E, 3.5°S-3.5°N]

(a) Location of the atmospheric indices

(g) LTS [8°-14°E, 5°S-5°N]

(f) U950 [12°-16°E, 4°S-eq]

FIGURE 15 (a) Location of the four boxes used to compute the atmospheric indices referred to in the other panels. In (b–g) the three left bars of each panel show full correlations between atmospheric variables (zonal wind (*U*) meridional wind (*V*) temperature (*T*) at the levels (in hPa) indicated in the subtitles as well as low tropospheric stability (LTS)) and PC#1 of diurnal types (Figure 7) as well as the two SST indices SAT and N34. Correspondingly, bar #4–5 of each panel show partial correlations without SAT, while bar #6–7 show partial correlations without N34. Grey and black bars indicate significant correlations at the two-sided 95% and 99% levels of significance, respectively according to a random-phase test (Ebisuzaki, 1997; Janicot et al., 1996) [Colour figure can be viewed at wileyonlinelibrary.com]

cloud cover and meridional winds at 950 and 850 hPa over the equatorial Atlantic adjacent to WEA. An increased stratiform cloudiness over WEA is associated with anomalous southerlies at low levels, combined with anomalous northerlies at 850 hPa, connecting anomalous upward motion around 7°N and anomalous subsidence over the equatorial Atlantic. Note that this anomalous low-level ascent around 5°–7°N is not associated with significant positive correlations between the leading PC of low-level clouds and JJAS seasonal rainfall. This discrepancy could be related to an intraseasonal modulation of this link, for example not peaking near the maximum of the JJAS rainfall. Nevertheless, this pattern is partly consistent with the shallow LLAC established with the

FIGURE 14 Correlations between the observed JJAS PC#1 of anomalous frequencies of the three diurnal types of stratiform cloud cover (Figure 8h) and (a) longitude-altitude (average of 0°-4° S) and (b) latitude-altitude (average of 9°–13°E) cross-sections of relative humidity (shading for significant correlations at the two-sided 95% level), temperature (blue and red contours for negative and positive significant correlations at the two-sided 95% level), zonal and vertical motions (vectors) on (a), meridional and vertical motions (vectors) on (b). For winds, the vectors are coloured in grey when correlations with either zonal or meridional and vertical winds are not significant at the two-sided 95% level. Green vectors show wind when any correlation is significant at the two-sided 95% level with width and darkness according to two thresholds (0.4 and 0.6). For clarity, vectors are shown every 2° of latitude and longitude. (c, d) Same as (a, b) except for -SAT. (e, f) Same as (a, b) except for N34 [Colour figure can be viewed at wileyonlinelibrary.com] development of the equatorial upwelling in May–June (Caniaux et al., 2011; de Coëtlogon et al., 2010). It is also not fully clear if the LLAC is simply a regional-scale fingerprint of the shallow meridional circulations across the tropical zone (Zhang et al., 2008). The extensive belt of negative correlations between WEA cloudiness and precipitation across the equatorial Atlantic and the Amazon Basin suggests that the mechanism operates at a larger scale than the LLAC, in connection with meridional shifts of the ITCZ.

The second mechanism involves the east–west thermal gradient between the equatorial cold tongue and the Congo Basin as well as the ENSO phenomenon. This mechanism is less clear for two different reasons: First, the E-W thermal gradient is controlled (among other factors) by both Equatorial Atlantic SST and ENSO, the warm and cold events of which do not necessarily coincide, therefore having either additional or counteracting effects on the zonal gradient across the Congo Basin. Second it is not clear if the vertical out-of-phase relation between the low and middle troposphere (i.e., more cloudy conditions with increased low-level westerlies and middle level easterlies over the Congo Basin) reflects a simple statistical covariation or a real 2D circulation cell. Anomalously cold SST over the equatorial Atlantic may promote more stratiform cloudiness, through intensified westerly advection of the cool and near-saturated air toward the Congo Basin. It should be noted that increased low-level westerlies may on the contrary promote clearing over the leeward mountains slopes east of 14°–15°E thus restricting the inland extension of both the JJAS mean stratiform cloud deck and the positive loadings of its leading EOF mode, which fluctuates around 15°E. However, there is almost no significant relationship between SAT and middle tropospheric winds in the zonal plane over the Congo Basin. In this layer, it is believed that the mechanism involves a greater control by ENSO, mostly through increased easterlies and broad warm anomalies during ENSO warm events. It is interesting to note that positive correlations between N34 and T700 over WEA peak when N34 leads T700 by a few months (not shown). Thus, ending (and prolonged) warm ENSO events may explain the subsequent mid-tropospheric warm anomalies, which play a role in WEA low clouds. The 700 hPa zonal winds also correlate with N34 but the correlation is highest at zero-lag, contrary to what is found for T700. By now, we have no physical explanation of this statistical result.

About a possible 2D zonal cell, it is not clear by now, if there is (and if so where) an ascending branch linking the low-level anomalous westerlies and middle/upper easterlies over the Congo Basin, since no significant positive relationship appears between LCF variations over WEA and rainfall over the central and eastern parts of the Congo Basin. So, at this stage, the statistical evidence is that, in the zonal plane, the thermodynamic characteristics of both the low and mid tropospheric levels, controlled probably by distinct forcings, are important factors.

The relationships between PC#1 and atmospheric variables related to stratiform cloudiness, with May SST indices of SAT and N34 help to detect some precursory signals. The relationship linking warm (cold) N34 anomalies and anomalous easterlies (westerlies), mostly in the middle and upper troposphere, is stronger when May SST are considered instead of JJAS SST. It is easy to understand that warm anomalies in the middle and upper troposphere, combined with cool low-level westerlies and possibly the increased vertical shear, may both increase LTS and thus lead to more or more frequent stratiform clouds over WEA. The temporal locking of the interactions between stratiform cloudiness and the equatorial and southern Atlantic is not as clear. But the JJAS atmospheric signals are already there in May, but these precursor SST signals are larger over the southeastern Atlantic off the coast of Angola than over the SAT area. This precursor SST signal may be due to the remote forcing by equatorial winds in boreal spring, which is well established on the occurrence of Atlantic Niños (Lübbecke et al., 2010). We may imagine some positive feedback since a thicker and/or more frequent stratiform cloud deck over the adjacent Atlantic, mostly driven by anomalously cold local SST anomalies, may also reduce the incoming solar radiation at the surface and thus support SST cooling.

6 | SUMMARY AND CONCLUDING REMARKS

The interannual variability of the stratiform cloud cover over WEA is investigated here using SYNOP observations (combining various sources and primarily based on the EECRA dataset; Champagne et al., 2023) and ERA5. The space–time variability of the stratiform cloud cover is first synthesized into three local diurnal types ("clear," "clear afternoon" and "cloudy" DTs). Their mean monthly variations suggest that the "clear afternoon" DT predominantly occurs at the margins (spatial and temporal) of the cloudiest area/cloudiest season. Interannual variations of the frequency of the three diurnal types show spatially consistent patterns, indicating that they are controlled by large-scale drivers. At the interannual scale, the "clear afternoon" type tends to be more in phase with the "clear" rather than the "cloudy" type during the cloudiest season JJAS. Afternoon low-level clouds are thus the most sensitive part of the diurnal cycle at the interannual time scale. This sensitivity fits well with the mean diurnal cycle in JJAS, which shows minimal LCF during the afternoon and early night (Champagne et al., 2023; Dommo et al., 2022). While the agreement between station diurnal types and their corresponding ERA5 grid-points is only moderate at daily time scale, the interannual variations are very similar over the cloudiest area of Gabon and southwestern RC represented by the leading JJAS principal component of the anomalous frequencies of the diurnal types. The interannual variations of the stratiform cloud cover during JJAS involves regional- and large-scale mechanisms; (1) a dominant influence associates air-sea coupling over the adjacent equatorial Atlantic upwelling region and its role in a shallow meridional cell and in the modulation of low-level westerlies over WEA; (2) the ENSO phenomenon is also involved, mostly through the modulation of thermal and wind anomalies mostly in and above the middle troposphere.

In future work, other potential drivers of low-level cloud cover variations should be investigated. One of them is the impact of biomass burning aerosols. The main fire season over the savannahs just south of the Congo Basin forests occurs during the austral winter, with a peak activity from June to September (De Sales et al., 2019; Solmon et al., 2021; Waquet et al., 2013), and wildfires produce large amounts of black carbon aerosols. These aerosols are partly advected above the low clouds toward the southern and equatorial Atlantic as well as WEA, by the prevailing easterly to southeasterly winds. They impact the local radiative balance and warm the mid-troposphere, causing a stabilization of the atmosphere that promotes the humidification of the cloud layer and leads also to longer-lived clouds (Costantino & Bréon, 2013; Fuchs et al., 2018; Solmon et al., 2021). Adebiyi and Zuidema (2018) showed that the aerosol loading increases the low-level cloud cover everywhere over the southeast Atlantic independent of meteorology, but that this positive relation is stronger farther offshore than near the coast north of 20°S, where the majority of the aerosol loading occurs. In particular, the positive aerosol–cloud relationship is rather weak off Gabon and RC. It must be stressed here that most of these previous studies focused on the aerosol–low cloud interaction over the sea.

Further work is also needed to better quantify the long-term trend of the low cloud cover, in particular to detect any signal related to anthropogenic global warming. The present results do not show any significant linear trend when the seasonal JJAS time scale is considered (weak positive nonsignificant trend for observed LCF and no trend for ERA5 LCF in Figure 8h), but monthly indexes of low-cloud cover over Gabon and SW RC (Figure 3) show contrasted long-term variations, that is, a weak (nonsignificant) increase in June–July, inconsistent trends between observed and ERA5 LCF in August and a significant decrease at the end of the cloudy season, especially in October. The absence of any significant long-term trend of low-level cloud cover in JJAS is by now rather puzzling, since the southern and equatorial Atlantic warming leads, in theory, to decreased stratiform cloud cover due to decreased LTS. First, removing the linear trend from SAT and BEN slightly increases the correlation with PC#1, corroborating the counteracting effect between interannual and long-term variations. The intra-annual modulation of the warming trend over SAT (maximum in October, then in May) fits also pretty well with the decreasing stratiform cloud cover noticed in Figure 4. The simple thermodynamical effect related to warmer SST offshore may be also counteracted for example by a stronger continental warming then increasing thermal land–sea contrast and associated atmospheric dynamics. Mid-tropospheric warming over WEA may also be possibly involved. Moreover, a specific analysis of the starting and ending stages of the cloudy season, adding other variables such as rainfall, would be a valuable addition to this work. Such analysis would also be helpful to analyse the nonlinear relationship between stratiform cloud and equatorial upwelling as observed by Fuchs et al. (2018). Further work is needed to understand the intraseasonal variability of the low cloud cover. In particular, it will be interesting to analyse the atmospheric conditions leading to intermittent clearings during the cloudy season, even over the core area of Gabon and SW RC. In order to address this issue, statistical analyses of low cloud cover and equatorial waves as well as numerical simulations focused on such intermittent clearings are currently underway.

AUTHOR CONTRIBUTIONS

Vincent Moron: Conceptualization; investigation; writing – original draft; methodology; validation; visualization; writing – review and editing; data curation. **P. Camberlin:** Conceptualization; investigation; methodology; validation; visualization; writing – review and editing; data curation. **R. Aellig:** Conceptualization; investigation; methodology; validation; visualization; writing – review and editing; data curation. **O. Champagne:** Conceptualization; investigation; methodology; validation; visualization; writing – review and editing; data curation. **A. H. Fink:** Conceptualization; investigation; funding acquisition;

writing – review and editing; visualization; validation; methodology; project administration; data curation; resources. **P. Knippertz:** Conceptualization; investigation; methodology; validation; visualization; writing – review and editing; data curation. **N. Philippon:** Conceptualization; investigation; funding acquisition; methodology; validation; visualization; writing – review and editing; data curation; project administration; resources.

ACKNOWLEDGEMENTS

This study is part of the project "Dynamics, Variability and Bioclimatic Effects of Low Clouds in Western Central Africa" (DYVALOCCA, https://dyvalocca.osug.fr/) funded by the French Agence Nationale de la Recherche (ANR) and the German Deutsche Forschungsgemeinschaft (DFG) from January 2020 to June 2023 under contract ANR-19-CE01-0021 and DFG FI 786/5-1, respectively, and to the International Joint Laboratory "Dynamics of land ecosystems in Central Africa in a context of global changes" of the Institut de Recherche pour le Développement (LMI DYCOFAC IRD, https://www.lmi-dycofac.org/).

DATA AVAILABILITY STATEMENT

All data used during this study are available from various open databases: EECRA is available on the 1971–2009 period from https://data.ucar.edu/dataset/extended-edited-synoptic-cloud-reports-archive-eecra-from-ships-and-land-stations-over-the-glob. SYNOP sources used to fill in and update EECRA LCF and LCG have been compiled from the ISD (https://www.ncei.noaa.gov/products/land-based-station/integrated-surface-database) and MIDAS databases (https://catalogue.ceda.ac.uk/uuid/220a65615218d5c9cc9e4785a3234bd0). GPCP monthly data is available from https://psl.noaa.gov/data/gridded/data.gpcp.html. ERA5 data have been extracted from the Copernicus repository (https://cds.climate.copernicus.eu/cdsapp#!/dataset/reanalysis-era5-pressure-levels?tab=overview).

REFERENCES

Adebiyi, A.A. & Zuidema, P. (2018) Low cloud cover sensitivity to biomass-burning aerosols and meteorology over the southeast Atlantic. *Journal of Climate*, 31, 4329–4346.

Adler, R.F., Sapiano, M.R.P., Huffman, G.J., Xie, P., Ferraro, R. & Shin, D.-B. (2018) The global precipitation climatology project (GPCP) monthly analysis (new version 2.3) and a review of 2017 global precipitation. *Atmosphere*, 9, 138. Available from: https://doi.org/10.3390/atmos9040138

Aellig, R., Moron, V., Camberlin, P., Champagne, O., Philippon, N., Fink, A.H. et al. (2022) *Cloud observing data of 85 stations in western Central Africa*. Karlsruhe: Karlsruher Institut für Technologie. Available from: https://doi.org/10.5445/IR/1000150635

Alexandersson, H. & Moberg, A. (1997) Homogenization of Swedish temperature data. Part I: homogeneity test for linear trends. *International Journal of Climatology*, 17, 25–34.

Bendix, J., Rütger Rollenbeck, R., Dietrich Göttlicher, D. & Cermak, J. (2006) Cloud occurrence and cloud properties in Ecuador. *Climate Research*, 30, 133–147.

Berrit, G.R. (1976) Les eaux froides côtières du Gabon à L'Angola sont-elles dues à un upwelling d'Ekman? *Cahier ORSTOM Séries Océanographie*, 14, 273–278.

Camberlin, P., Togbedji, C.F., Pergaud, J., Berger, A., Aellig, R., Fink, A.H. et al. (2023) The representation of dry-season low-level clouds over western equatorial Africa in reanalyses and historical CMIP6 simulations. *Climate Dynamics* (in press). Available from: https://doi.org/10.1007/s00382-023-06714-w

Caniaux, G., Giordani, H., Redelsperger, J.-L., Guichard, F., Key, E. & Wade, M. (2011) Coupling between the Atlantic cold tongue and the West African monsoon in boreal spring and summer. *Journal of Geophysical Research: Atmosphere*, 116, C04003. Available from: https://doi.org/10.1029/2010JC006570

Champagne, O., Aellig, R., Fink, A.H., Philippon, N., Camberlin, P., Moron, V. et al. (2023) Main dry season low cloud cover climatology in western equatorial Africa: comparison between ground observations and satellites. *Journal of Climate*, 36, 4289–4306.

Cook, K.H. & Vizy, E.K. (2016) The Congo Basin Walker circulation: dynamics and connections to precipitation. *Climate Dynamics*, 47, 697–717.

Costantino, L. & Bréon, F.M. (2013) Aerosol indirect effect on warm clouds over South-East Atlantic, from co-located MODIS and CALIPSO observations. I. *Atmospheric Chemistry and Physics*, 13, 69–88. Available from: https://doi.org/10.5194/acpd-12-14197-2012

de Coëtlogon, G., Janicot, S. & Lazar, A. (2010) Intraseasonal variability of the ocean–atmosphere coupling in the Gulf of Guinea during boreal spring and summer. *Quarterly Journal of the Royal Meteorological Society*, 136, 426–441.

De Sales, F., Okin, G.S., Xue, Y. & Dintwe, K. (2019) On the effects of wildfires on precipitation in southern Africa. *Climate Dynamics*, 52, 951–967.

Dommo, A., Philippon, N., Vondou, A.D., Sèze, G. & Eastman, R. (2018) The June–September low cloud cover in western Central Africa: mean spatial distribution and diurnal evolution, and associated atmospheric dynamics. *Journal of Climate*, 31, 9585–9603.

Dommo, A., Voundou, D.A., Philippon, N., Eastman, R., Moron, V. & Aloysius, N. (2022) The ERA5's diurnal cycle of low-level clouds over Western Central Africa during June–September: dynamic and thermodynamic processes. *Atmospheric Research*, 280, 106426.

Eastman, R. & Warren, S.G. (2013) A 39-yr survey of cloud changes from land stations worldwide 1971–2009: long-term trends, relation to aerosols, and expansion of the Tropical Belt. *Journal of Climate*, 26, 1286–1303.

Eastman, R. & Warren, S.G. (2014) Diurnal cycles of cumulus, cumulonimbus, stratus, stratocumulus, and fog from surface observations over land and ocean. *Journal of Climate*, 27, 2386–2404.

Eastman, R., Warren, S.G. & Hahn, C.J. (2011) Variations in cloud cover and cloud types over the ocean from surface observations, 1954–2008. *Journal of Climate*, 24, 5914–5934.

Ebizusaki, W. (1997) A method to estimate the statistical significance of a correlation when the data are serially correlated. *Journal of Climate*, 10, 2147–2153.

Fuchs, J., Cermak, J. & Andersen, H. (2018) Building a cloud in the southeast Atlantic: understanding low-cloud controls based on satellite observations with machine learning. *Atmospheric Chemistry and Physics*, 18, 16537–16552.

Hahn, C.J. & Warren, S.G. (2009) Extended edited synoptic cloud reports from ships and land stations over the globe, 1952–1996 (2009 update). CDIAC Numerical Data Package, NDP-026C, 79 pp.

Hersbach, H., Bell, B., Berrisford, P., Hirahara, S., Horányi, A., Muñoz-Sabater, J. et al. (2020) The ERA5 global reanalysis. *Quarterly Journal of the Royal Meteorological Society*, 146, 1999–2049.

Janicot, S., Moron, V. & Fontaine, B. (1996) Sahel drought and ENSO dynamics. *Geophysical Research Letters*, 23, 515–518.

Katz, R.W. & Glantz, M.H. (1986) Anatomy of a rainfall index. *Monthly Weather Review*, 114, 764–771.

Khaliq, M.N. & Ouarda, T.B. (2007) On the critical values of the standard normal homogeneity test (SNHT). *International Journal of Climatology*, 27, 681–687.

Klein, S.A. & Hartmann, D.L. (1993) The seasonal cycle of low stratiform clouds. *Journal of Climate*, 6, 1587–1606.

Klein, S.A., Hartmann, D.L. & Norris, J.R. (1995) On the relationships among low-cloud structure, sea surface temperature, and atmospheric circulation in the summertime Northeast Pacific. *Journal of Climate*, 8, 1140–1155.

Knippertz, P., Fink, A.H., Schuster, R., Trentmann, J., Schrage, J.M. & Yorke, C. (2011) Ultra-low clouds over the southern WestAfrican monsoon region. *Geophysical Research Letters*, 38, L21808.

Koshiro, T. & Shiotani, M. (2014) Relationship between low stratiform cloud amount and estimated inversion strength in the lower troposphere over the global ocean in terms of cloud types. *Journal of the Meteorological Society of Japan*, 92, 107–120.

Leduc-Leballeur, M., de Coëtlogon, G. & Eymard, L. (2013) Air–sea interaction in the Gulf of Guinea at intraseasonal timescales: wind bursts and coastal precipitation in boreal spring. *Quarterly Journal of the Royal Meteorological Society*, 139, 992–1003.

Li, T. & Philander, S.G.H. (1997) On the seasonal cycle of the equatorial Atlantic Ocean. *Journal of Climate*, 10, 813–817.

Longandjo, G.N.T. & Rouault, M. (2020) On the structure of the regional-scale circulation over Central Africa: seasonal evolution, variability, and mechanisms. *Journal of Climate*, 33, 145–162.

Lübbecke, J.F., Böning, C.W., Keenlyside, N.S. & Xie, S.P. (2010) On the connection between Benguela and equatorial Atlantic Niños and the role of the South Atlantic anticyclone. *Journal of Geophysical Research: Oceans*, 115(C9), C09015.

Merle, J., Fieux, M. & Hisard, P. (1979) Annual signal and interannual anomalies of sea surface temperature in the eastern equatorial Atlantic Ocean. *Deep Sea Research*, 26, 77–102.

Meynadier, R., De Coëtlogon, G., Leduc-Leballeur, M., Eymard, L. & Janicot, S. (2016) Seasonal influence of the sea surface temperature on the low atmospheric circulation and precipitation in the eastern equatorial Atlantic. *Climate Dynamics*, 47, 1127–1142.

Michelangeli, P.A., Vautard, R. & Legras, B. (1995) Weather regimes: recurrence and quasi-stationarity. *Journal of Atmospheric Sciences*, 52, 1237–1256.

Moore, D., Hisard, P., McCreary, J., Merle, J., O'Brien, J., Picaut, J. et al. (1978) Equatorial adjustment in the eastern Atlantic. *Geophysical Research Letters*, 5, 637–640.

Neupane, N. (2016) The Congo Basin zonal overturning circulation. *Advances in Atmospheric Sciences*, 33, 767–782.

Nicholson, S.E. & Grist, J.P. (2003) The seasonal evolution of the atmospheric circulation over West Africa and equatorial Africa. *Journal of Climate*, 16, 1013–1030.

Norris, J.R. (1998a) Low cloud type over the ocean from surface observations. Part I: relationship to surface meteorology and the vertical distribution of temperature and moisture. *Journal of Climate*, 11, 369–382.

Norris, J.R. (1998b) Low cloud type over the ocean from surface observations. Part II: geographical and seasonal variations. *Journal of Climate*, 11, 383–403.

Norris, J.R. & Leovy, C.B. (1994) Interannual variability in stratiform cloudiness and sea surface temperatures. *Journal of Climate*, 7, 1915–1925.

Oreopoulos, L. & Davies, R. (1993) Statistical dependence of albedo and cloud cover on sea surface temperature for two tropical marine stratocumulus regions. *Journal of Climate*, 6, 2434–2447.

Osborn, T.J., Briffa, K.R. & Jones, P.D. (1997) Adjusting variance for sample-size in tree-ring chronologies and other regional mean timeseries. *Dendrochronologia*, 15, 89–99.

Park, S. & Leovy, C.B. (2004) Marine low-cloud anomalies associated with ENSO. *Journal of Climate*, 17, 3448–3469.

Philippon, N., Cornu, G., Monteil, L., Gond, V., Moron, V., Pergaud, J. et al. (2019) The light-deficient climates of western Central African evergreen forests. *Environmental Research Letters*, 14, 034007.

Philippon, N., de Lapparent, B., Gond, V., Sèze, G., Martiny, N., Camberlin, P. et al. (2016) Analysis of the diurnal cycles for a better understanding of the mean annual cycle of forests greenness in Central Africa. *Agricultural and Forest Meteorology*, 223, 81–94.

Philippon, N., Ouhechou, A., Camberlin, P., Trentmann, J., Fink, A.H., Maloba, J.D. et al. (2022) Characterization of sunshine duration in western equatorial Africa: in-situ measurements vs SARAH-2 satellite estimates. *Journal of Applied Meteorology and Climatology*, 61, 185–201.

Picaut, J. (1983) Propagation of the seasonal upwelling in the eastern equatorial Atlantic. *Journal of Physical Oceanography*, 13, 18–36.

Pokam, M.W., Bain, C.L., Chadwick, R.S., Graham, R., Sonwa, D.J. & Kamga, F.M. (2014) Identification of processes driving low-level westerlies in west equatorial Africa. *Journal of Climate*, 27, 4245–4262.

Réjou-Méchain, M., Mortier, F., Bastin, J.-F., Cornu, G., Barbier, N., Bayol, N. et al. (2021) Unveiling African rainforest composition and vulnerability to global change. *Nature*, 593, 90–94.

Solmon, F., Eguindi, N., Mallet, M., Flamant, C. & Fomenti, P. (2021) West African monsoon precipitation impacted by the south eastern Atlantic biomass burning aerosol outflow. *npj Climate and Atmospheric Science*, 4, 54.

Sultan, B. & Janicot, S. (2003) The West African monsoon dynamics. Part II. The “preonset” and “onset” of the summer monsoon. *Journal of Climate*, 16, 3407–3427.

Tibshirani, R., Walther, G. & Hastie, T. (2001) Estimating the number of clusters in a data set via the gap statistic. *Journal of the Royal Statistical Society*, B63, 411–423.

Trenberth, K.E. & Smith, L. (2006) The vertical structure of temperature in the tropics: different flavors of El Niño. *Journal of Climate*, 19, 4956–4973.

van der Linden, R., Fink, A.H. & Redl, R. (2015) Satellite-based climatology of low-level continental clouds in southern West Africa during the summer monsoon season. *Journal of Geophysical Research: Atmosphere*, 120, 1186–1201.

Wang, L.C., Jin, F.F., Wu, C.R. & Hsu, H.H. (2017) Dynamics of upwelling annual cycle in the equatorial Atlantic Ocean. *Geophysical Research Letters*, 44, 3737–3743.

Waquet, F., Peers, F., Ducos, F., Goloub, P., Platnick, S., Riedi, J. et al. (2013) Global analysis of aerosol properties above clouds. *Geophysical Research Letters*, 40, 5809–5814.

Weare, B.C. (2000) Near-global observations of low clouds. *Journal of Climate*, 13, 1255–1268.

Wood, R. (2012) Stratocumulus clouds. *Monthly Weather Review*, 140, 2373–2423.

Wood, R. & Bretherton, C.S. (2006) On the relationship between stratiform low cloud cover and lower-tropospheric stability. *Journal of Climate*, 19, 6425–6432.

Yulaeva, E. & Wallace, J.M. (1994) The signature of ENSO in global temperature and precipitation fields derived from the microwave sounding unit. *Journal of Climate*, 7, 1719–1736.

Zhang, C., Nolan, D.S., Thorncroft, C.D. & Nguyen, H. (2008) Shallow meridional circulations in the tropical atmosphere. *Journal of Climate*, 21, 3453–3470.

Zhang, Y., Stevens, B., Medeiros, B. & Ghil, M. (2009) Low-cloud fraction, lower-tropospheric stability, and large-scale divergence. *Journal of Climate*, 22, 4827–4844.

How to cite this article: Moron, V., Camberlin, P., Aellig, R., Champagne, O., Fink, A. H., Knippertz, P., & Philippon, N. (2023). Diurnal to interannual variability of low-level cloud cover over western equatorial Africa in May–October. *International Journal of Climatology*, 1–27. https://doi.org/10.1002/joc.8188